

Simulating the tidal disruption of stars by stellar-mass black holes using moving-mesh hydrodynamics

Pavan Vynatheya^{1,*}, Taeho Ryu^{1,2}, Rüdiger Pakmor¹, Selma E. de Mink^{1,3} and Hagai B. Perets⁴

¹ Max-Planck-Institut für Astrophysik, Karl-Schwarzschild-Straße 1, 85748 Garching bei München, Germany

² Physics and Astronomy Department, Johns Hopkins University, Baltimore, MD 21218, USA

³ Anton Pannekoek Institute for Astronomy, University of Amsterdam, Science Park 904, 1098 XH Amsterdam, Netherlands

⁴ Physics Department, Technion - Israel Institute of Technology, Haifa 3200003, Israel

Received XXX; accepted YYY

ABSTRACT

In the centers of dense star clusters, close encounters between stars and compact objects are likely to occur. We study tidal disruption events of main-sequence (MS) stars by stellar-mass black holes (termed μ TDEs), which can shed light on the processes occurring in these clusters, including being an avenue in the mass growth of stellar-mass BHs. Using the moving-mesh hydrodynamics code AREPO, we perform a suite of 58 hydrodynamics simulations of partial μ TDEs of realistic, MESA-generated MS stars by varying the initial mass of the star ($0.5 M_{\odot}$ and $1 M_{\odot}$), the age of the star (zero-age, middle-age and terminal-age), the mass of the black hole ($10 M_{\odot}$ and $40 M_{\odot}$) and the impact parameter (yielding almost no mass loss to full disruption). We then examine the dependence of the masses, spins, and orbital parameters of the partially disrupted remnant on the initial encounter parameters. We find that the mass lost from a star decreases roughly exponentially with increasing distance of approach and that a $1 M_{\odot}$ star loses lesser mass than a $0.5 M_{\odot}$. Moreover, a more evolved star is less susceptible to mass loss. Tidal torques at the closest approach spin up the remnant very close to break-up velocity when the impact parameter is low. The remnant star can be bound (eccentric) or unbound (hyperbolic) to the black hole: hyperbolic orbits occur when the star's central density concentration is relatively low and the black hole-star mass ratio is high, which is the case for the disruption of a $0.5 M_{\odot}$ star. Finally, we provide best-fit analytical formulae for the aforementioned range of parameters that can be incorporated into cluster codes to model star-black hole interaction more accurately.

Key words. stars: kinematics and dynamics – black hole physics – hydrodynamics – gravitation

1. Introduction

Tidal disruption events (TDEs) of stars by supermassive black holes (SMBHs) have been a subject of significant interest in the past decade (see Stone et al. 2019; Gezari 2021 for reviews). TDEs by SMBHs are observed as transients in multiple wavelengths (Gezari 2021), with ~ 100 such events having been detected by observatories in optical (ASAS-SN: Kochanek et al. 2017, ZTF: Bellm et al. 2019, PTF: Law et al. 2009, PS: Chambers et al. 2016, ATLAS: Tonry et al. 2018, SDSS: Kollmeier et al. 2019, OGLE: Udalski et al. 2015), X-ray (ROSAT: Voges et al. 1999, Swift: Gehrels et al. 2004, XMM: Jansen et al. 2001, Chandra: Weisskopf et al. 2000) and UV (GALEX: Martin et al. 2005).

In this work, we examine TDEs of stars by stellar-mass black holes or SBHs (termed μ TDEs). These are less studied and have only garnered interest recently. Although μ TDEs have lower observable rates (Perets et al. 2016), they can shed light on the processes occurring in the centers of globular and nuclear star clusters where they are most likely to occur. In particular, they are an important avenue in the mass growth of SBHs to form intermediate-mass black holes (IMBHs, e.g., Stone et al. 2017; Rizzuto et al. 2023). However, these studies make simplistic assumptions about the mass accreted onto a black hole after a TDE, which highlights the need for detailed simulations to model this interaction more accurately for the next generation of globular

cluster simulations. Partial tidal disruptions (PTDEs), which are more likely than full tidal disruptions (FTDEs), can be responsible for the tidal capture, and subsequent encounters, of the remnant star by the BH if the remnant ends up in a bound orbit. The remnant stars of such interactions tend to be spun up from the torque due to the BH and can have peculiar internal structures (e.g., Alexander & Kumar 2001).

μ TDEs are also of interest in the context of low-mass X-ray binaries (LMXBs) and the newly-discovered Gaia BHs (El-Badry et al. 2023a,b; Chakrabarti et al. 2023). Isolated binary evolution cannot satisfactorily explain the observed rates of binaries with BHs and low-mass stellar companions (e.g., Podsiadlowski et al. 2003; Kiel & Hurley 2006). Hence, the dynamical formation of such binaries in clusters, through PTDEs and subsequent tidal captures, may very well be a crucial process to explain them.

Accurate modeling of post-disruption orbits and the internal structure of remnant stars requires detailed hydrodynamics simulations. The first detailed study on μ TDEs was carried out by Perets et al. (2016). They estimated that these events could occur in Milky Way globular clusters at a rate of $10^{-6} \text{ yr}^{-1} \text{ MWGal}^{-1}$, and might observationally resemble ultra-long GRB events. Similar rates were obtained for scenarios where a supernova natal kick to a newly formed BH results in a chance encounter with its binary companion. Wang et al. (2021) used smoothed-particle hydrodynamics (SPH) to find the fallback rates onto the BH in the case of partial μ TDEs of polytropic stars. Kremer et al.

* corresponding author

(2022) performed a large suite of SPH simulations of partial- and full-disruptions, with varying BH and stellar masses, stellar polytropic indices, and impact parameters. Among other things, they observed that stellar structure plays a crucial role in the boundedness of the remnant stars after partial disruption, with the possibility of less centrally ‘concentrated’ stars ending up in hyperbolic orbits. [Xin et al. \(2024\)](#) looked at low-eccentricity ‘tidal-peeling’ events of realistic MS stars, with the star being slowly stripped away in multiple orbits.

Hydrodynamics studies on three-body encounters involving SBHs in globular clusters have also garnered interest, motivated by the significantly larger cross-sections of binary-single tidal interactions. [Lopez et al. \(2019\)](#) studied the interaction of binary BHs and polytropic stars and showed that tidal disruption can alter the spin of one of the BHs. An extensive series of studies was carried out by [Ryu et al. \(2022, 2023a,b, 2024b\)](#), using both SPH and moving-mesh codes, on the different combinations of close encounters between realistic MS stars and SBHs.

In our study, we use the moving-mesh code AREPO ([Springel 2010; Pakmor et al. 2016; Weinberger et al. 2020](#)) to simulate μ TDEs of low-mass MS stars with SBHs. It should be noted that [Ryu et al. \(2023a,b, 2024b\)](#) also employed AREPO to model TDEs with remarkable success. We generate realistic stellar models from detailed 1D MESA ([Paxton et al. 2011](#)) profiles. TDEs of MESA-generated stars by SMBHs and IMBHs have been investigated in the past (e.g., [Gallegos-Garcia et al. 2018; Golightly et al. 2019; Law-Smith et al. 2019, 2020; Ryu et al. 2020a,b,c,d; Kiroglu et al. 2023](#)), but μ TDE studies have typically probed polytropic stars. In this paper, we focus on the dependence of post-disruption mass, spin, and orbital parameters on the initial conditions and provide best-fit functions for the same. These fits can be incorporated into N -body or other cluster codes for better treatment of star-BH encounters.

The paper is organized as follows. In Section 2, we detail our simulation methodology, including our grid of initial conditions. We briefly describe the analysis of certain quantities in Section 3 and present our results and best-fit functions in Section 4. Section 5 and Section 6 discuss the implications of our work and conclude, respectively.

2. Methods

2.1. Hydrodynamics

We simulate the disruption of stars by black holes using the moving-mesh magnetohydrodynamics code AREPO ([Springel 2010; Pakmor et al. 2016; Weinberger et al. 2020](#)). AREPO is a massively parallel 3D magnetohydrodynamics code with gravity that inherits many advantages of the two popular schemes, Eulerian grid-based finite-volume codes and Lagrangian smoothed particle hydrodynamics (SPH). Although initially developed for cosmological simulations, AREPO has been successfully employed in phenomena involving stars, e.g., tidal disruptions and encounters ([Goicovic et al. 2019; Ryu et al. 2023a,b, 2024b](#)), TDEs in active galactic nuclei disks ([Ryu et al. 2024c](#)), collisions of main-sequence stars ([Schneider et al. 2019](#)), giant stars ([Ryu et al. 2024a](#)), white dwarfs ([Pakmor et al. 2013, 2021, 2022; Burmester et al. 2023; Gronow et al. 2021; Glanz et al. 2023](#)) and neutron stars ([Lioutas et al. 2024](#)), and common envelope evolution ([Ohlmann et al. 2016a,b; Sand et al. 2020; Kramer et al. 2020; Ondratschek et al. 2022](#)).

To solve the fluid equations, AREPO builds an unstructured Voronoi mesh with cells of varying volume and calculates fluxes between the cells in a finite-volume approach. The Voronoi mesh

Table 1: Parameters of the $Z_{\star} = 0.02$ MS star models.

m_{\star} [M_{\odot}]	t_{\star} [Gyr]	H_c	r_{\star} [R_{\odot}]	$t_{\text{dyn},\star}$ [hr]	ρ_{conc}^{-1}
0.5	0.01	0.70	0.44	0.19	0.46
	0.01	0.70	0.90	0.38	0.29
1.0	4.68	0.34	1.02	0.46	0.20
	8.60	0.00	1.22	0.60	0.12

Notes. The columns indicate stellar parameters - the mass m_{\star} , the age t_{\star} , the central hydrogen abundance H_c , the radius r_{\star} , the dynamical time $t_{\text{dyn},\star}$ and the inverse of the density concentration parameter ρ_{conc}^{-1} .

moves in time according to the approximate bulk velocities of the fluid elements. Gravity is handled in a tree-particle-mesh scheme (see [Bagla 2002](#)), with the minimum gravitational softening for the gas (star) cells set as one-tenth of the smallest gas cell for accuracy. AREPO allows for adaptation of spatial resolution according to arbitrary criteria on top of the default adaptivity to density, inherited from the near-Lagrangian nature of the scheme. It also includes particles that interact only gravitationally. We assume Newtonian gravity and do not include magnetic fields in our simulations.

2.2. Stellar models

We use the 1D stellar modeling code MESA ([Paxton et al. 2011](#)) to generate main-sequence (MS) stellar models with initial masses $m_{\star} = 0.5 M_{\odot}$ and $1.0 M_{\odot}$, and metallicity $Z_{\star} = 0.02$ (near-solar) at different ages. These masses are typical for globular clusters that predominantly consist of old, low-mass stars (e.g., [Salaris & Weiss 2002; De Angeli et al. 2005; Marín-Franch et al. 2009](#)), while the metallicity is higher than those of most clusters, which typically have a tenth (or less) of Solar metallicity (e.g., [Harris 2010](#)). However, the effect of metallicity is not expected to be significant and is quantified in Section 4. MESA solves the stellar structure equations to compute the evolution and provides us with stellar mass- and radial-profile parameters (e.g., densities, temperatures, and chemical abundances) at different evolutionary phases. We convert these 1D profiles to 3D AREPO initial conditions using the scheme adopted by [Ohlmann et al. \(2017\)](#), with the Helmholtz equation of state ([Timmer & Swesty 2000](#)). After generating the star, we relax it for five stellar dynamical timescales $t_{\text{dyn},\star} = (r_{\star}^3/Gm_{\star})^{0.5}$, where r_{\star} is the stellar radius and G is the gravitational constant. We then use this relaxed star for the disruption simulations.

Stellar density profiles are a major factor in determining whether a star undergoes a partial tidal disruption (PTDE) or a full tidal disruption (FTDE) for a given periastris distance (e.g., [Ryu et al. 2020c](#)). To that end, we consider MESA models of three evolutionary stages of $1.0 M_{\odot}$ MS stars with varying core hydrogen abundances H_c , which correspond to distinct density profiles (see also [Gallegos-Garcia et al. 2018; Golightly et al. 2019; Law-Smith et al. 2019; Goicovic et al. 2019](#)). The first is close to the onset of hydrogen burning ($H_c \approx 0.70$), i.e., zero-age main-sequence (hereafter ZAMS), the second is approximately midway through the main-sequence ($H_c \approx 0.34$), i.e., middle-age main-sequence (hereafter MAMS), and the third is close to the depletion of core hydrogen ($H_c \approx 0.00$), i.e., terminal-age main-sequence (hereafter TAMS). The total stellar mass remains nearly constant throughout the MS lifetime owing to the insignificant wind mass loss. In the case of the $0.5 M_{\odot}$ stars, we exam-

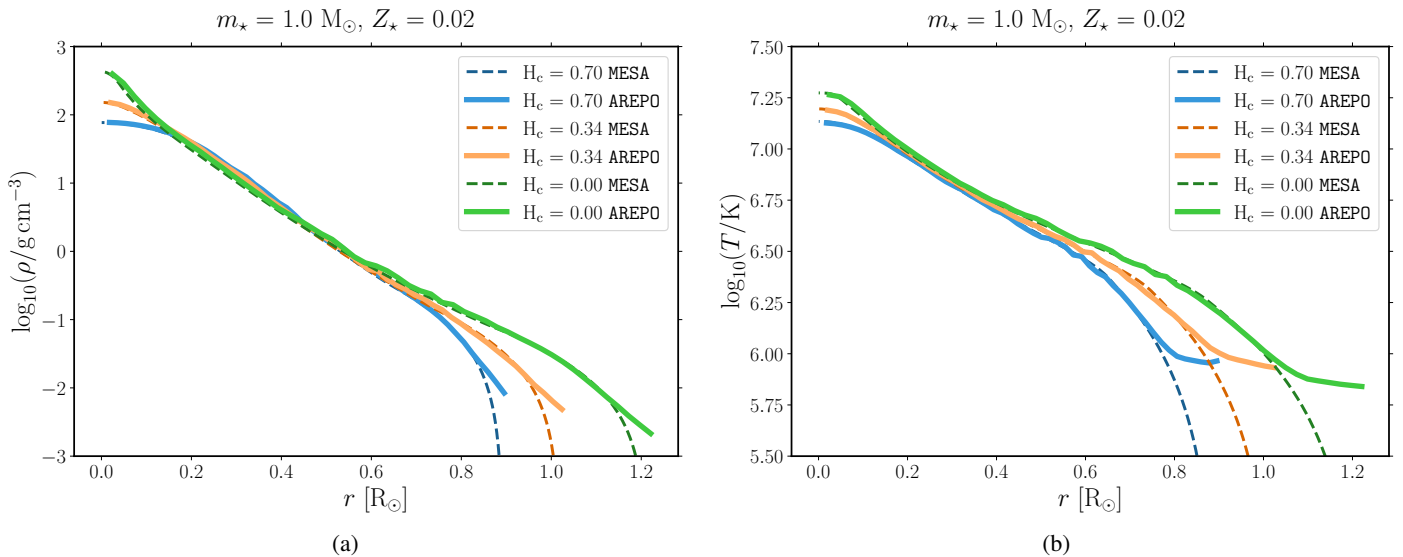


Fig. 1: Density (left) and temperature (right) profiles of a $1 M_{\odot}$ MS star of different models (see Table 1). The dashed and solid lines represent the 1D profiles generated by MESA and initialized (and subsequently relaxed for five dynamical timescales) in 3D in AREPO respectively. They agree very well over most of the range except close to the stellar surface because of smoothing during relaxation in AREPO. An older MS star (with lower H_c) has a denser and hotter core and a puffier outer layer than a younger MS star (with higher H_c).

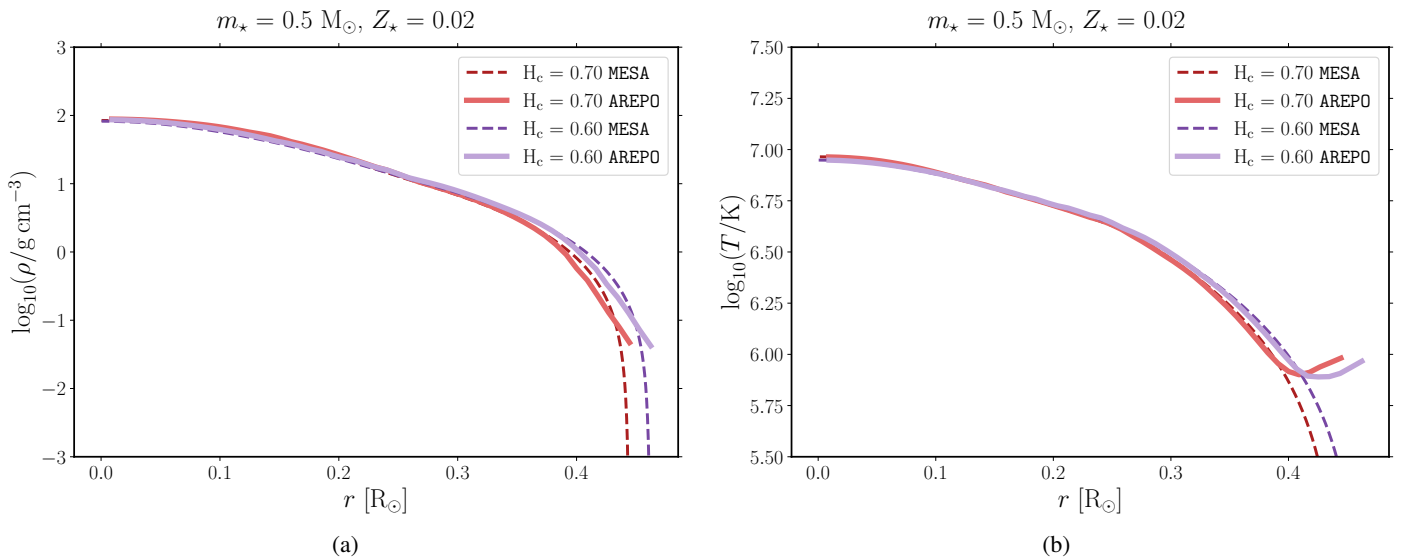


Fig. 2: Similar profiles as Figure 1, but for a $0.5 M_{\odot}$ MS star. A $0.5 M_{\odot}$ star of age ~ 13.5 Gyr with $H_c = 0.60$ (purple curves) is very similar to a ZAMS star with $H_c = 0.70$ (red curves), albeit with a slightly larger radius.

ine only ZAMS profiles ($H_c \approx 0.70$). This choice is motivated by the fact that their internal structure barely changes over time (see Figure 2) owing to their large MS lifetimes. One could choose a $0.5 M_{\odot}$ star at an age comparable to a Hubble time (e.g., Ryu et al. 2020a,c) but the results are expected to be very similar. Table 1 lists the stellar parameters of the MS star models for the stellar masses and ages we simulate.

Furthermore, we performed resolution scaling tests to ensure that the PTDE simulations were robust. To this end, we varied the number of fluid (star) cells making up a $1 M_{\odot}$ star – 5×10^4 , 8×10^4 , 2×10^5 , 5×10^5 , and 8×10^5 . We then performed PTDE simulations involving a $1 M_{\odot}$ star and a $10 M_{\odot}$ BH for each resolution. The masses lost due to tidal disruption plateaued close to the resolutions 2×10^5 and 5×10^5 , with the mass loss val-

ues using 5×10^5 and 8×10^5 cells being essentially the same. Hence, we chose an initial resolution of 5×10^5 fluid cells for the stars in this study. It should be noted that the number of cells increases as the simulations progress since AREPO automatically adds extra cells when the density gradient is high.

Figure 1 shows that more evolved $1 M_{\odot}$ MS stars have a denser (left panel) and hotter (right panel) core and a puffier outer layer than less evolved MS stars. Since the three stars have different radii r_{\star} , they also have different $t_{\text{dyn},\star}$ and different tidal radii $r_t = (m_{\text{BH}}/m_{\star})^{1/3} r_{\star}$ for the same BH mass m_{BH} . Figure 2 shows that $0.5 M_{\odot}$ stars of different ages – ZAMS ($H_c = 0.70$) and ~ 13.5 Gyr ($H_c = 0.60$) – have very similar density and temperature profiles, which justifies excluding the latter from our simulation runs. It should be noted that the AREPO profiles, espe-

Table 2: Initial parameters of our suite of simulations.

m_\star [M_\odot]	m_{BH} [M_\odot]	H_c	$b = r_p/r_t$
0.5	10.0, 40.0	0.70	0.25, 0.33, 0.50, 0.75, 1.00, 1.50, 2.00, 2.50
1.0	10.0, 40.0	0.70, 0.34, 0.00	0.25, 0.33, 0.50, 0.75, 1.00, 1.50, 2.00

Notes. The columns indicate the initial parameters - the stellar mass m_\star , the BH mass m_{BH} , the core hydrogen fraction H_c , and the impact parameter b . In each row, every comma-separated combination of values in all columns is simulated, to give a total of 58 simulations.

cially the temperature, diverge significantly from the MESA ones near the surface of the star (corresponding to a fractional mass of $\sim 10^{-4}$ – 10^{-3}). This amount of mass near the surface that deviates from the MESA model sets the minimum amount of stripped mass in PTDEs that we can resolve. Therefore, we only present the results of PTDEs yielding a mass loss $\gtrsim 10^{-4}m_\star$ in this paper.

2.3. Black hole

The black holes are initialized in AREPO as non-rotating sink particles that interact gravitationally and grow in mass through accretion. We set the gravitational softening length of the BH to be ten times the minimum softening length of the gas (star) cells. The scheme we use for accretion onto the BH, described here briefly, is the same as the one used in Ryu et al. (2022, 2023a,b, 2024b). Firstly, the cells around the BH within a radius of $10^4 r_g$, where gravitational radius $r_g = Gm_{\text{BH}}/c^2$, are identified. Secondly, the accretion onto the BH is calculated using a weighted average of radial flux to account for the higher contribution of gas closer to the BH and vice-versa. Thirdly, mass is extracted from the neighboring cells of the BH, and momentum is inserted in the BH to conserve these quantities. Finally, the BH is spun up from accretion by adding angular momentum from the selected neighboring cells. The radiation feedback from accretion is not taken into account. Although angular momentum is conserved through this scheme, there is no guarantee that the total energy is conserved. However, given that accretion onto the black hole is small in our simulations, the energy lost due to accretion is negligible.

We run simulations with SBH masses of $10 M_\odot$ and $40 M_\odot$, which are in proximity to the lower- and higher-mass peaks of observed LIGO BH masses (e.g., Abbott et al. 2021, 2023). Given the mass of the BH m_{BH} , the mass of the star m_\star , and the radius of the star r_\star , the classical tidal radius is defined as $r_t = (m_{\text{BH}}/m_\star)^{1/3} r_\star$.

2.4. Initial conditions

The distance of the closest approach is characterized by the impact parameter: $b \equiv r_p/r_t$ ¹, where r_p is the periapsis distance of the initially parabolic orbit. We vary the mass of the star: $0.5 M_\odot$ and $1 M_\odot$, and the mass of the black hole: $10 M_\odot$ and $40 M_\odot$. We then generate a suite of simulations of b varying from 0.25 to 2.00 ($1 M_\odot$ stars) or 2.50 ($0.5 M_\odot$ stars), and the three stellar ages (density profiles) to determine the post-disruption orbital, mass and spin parameter. The additional simulations for $0.5 M_\odot$ and $b = 2.50$ are performed to properly analyze the PTDE trends since $0.5 M_\odot$ stars are fully disrupted for $b \lesssim 1.00$.

¹ $\beta \equiv b^{-1}$ is often introduced in the literature for TDEs by SMBHs as the ‘penetration factor’.

We also assume that the initial stars are non-rotating and that the star-BH encounters are parabolic. This can be justified for encounters in globular clusters because the velocity dispersions of Milky Way globular clusters are in the range ~ 1 – 20 km s^{-1} (e.g., Baumgardt & Hilker 2018). For instance, given a velocity dispersion $\sigma \approx 10 \text{ km s}^{-1}$, $|1 - e| \approx 10^{-4}$ (very close to parabolic) for the parameters considered in this paper.

Each simulation is run for $\sim 70 t_{\text{dyn},\star}$ after periapsis passage. This duration was chosen to ensure that the stellar masses reach steady values for proper analysis. Table 2 provides an overview of the parameters we use in our suite of simulations.

3. Analysis

3.1. Calculation of bound and unbound mass

To find the center of mass of a self-bound object (i.e., star before disruption, remnant after disruption) in each snapshot, we used an iterative procedure fairly similar to Guillochon & Ramirez-Ruiz (2013), with some differences to improve the accuracy of the identification of bound and unbound cells. For each snapshot, we chose the gas cell with the maximum density as the ‘initial’ guess for the center of mass (CoM) position. Subsequently, we calculate the specific total energies of all the star cells relative to the star CoM, $\epsilon_{\text{cell,CoM}}$, and the BH, $\epsilon_{\text{cell,BH}}$, as the sum of their relative kinetic, potential and internal energies. We consider a cell to be bound to a self-gravitating object if $\epsilon_{\text{cell,CoM}} < 0$, $\epsilon_{\text{cell,CoM}} < \epsilon_{\text{cell,BH}}$. The last condition ensures that the cells bound to the star are ‘close’ to the CoM. We compute a ‘new’ CoM position (and velocity) using these bound cells and determine the ‘new’ specific energy. We iterate this process until there is no change in the relative position of the CoM. Subsequently, we calculate its ‘final’ bound mass. In the case of an FTDE, we also visually inspect the surface density plots and assign the mass bound to the star to be zero.

The mass bound to the BH is calculated in a similar fashion, though the position of the BH is trivially known from the simulation. Finally, we consider any cells with $\epsilon_{\text{cell,CoM}} \geq 0$ and $\epsilon_{\text{cell,CoM}} \geq 0$ unbound from the system.

3.2. Calculation of orbital and spin parameters

For each snapshot post-disruption, we compute the instantaneous Keplerian orbital parameters – the semimajor axis a and orbital eccentricity e – using the current values of the mass bound to the star m_\star , the mass of the BH (plus the gas mass bound to it) m_{BH} , the positions and velocities of the star’s CoM ($\mathbf{r}_{\text{CoM}}, \mathbf{v}_{\text{CoM}}$) and the BH ($\mathbf{r}_{\text{BH}}, \mathbf{v}_{\text{BH}}$). For completeness, with $\mathbf{r} \equiv \mathbf{r}_{\text{CoM}} - \mathbf{r}_{\text{BH}}$ and $\mathbf{v} \equiv \mathbf{v}_{\text{CoM}} - \mathbf{v}_{\text{BH}}$, the equations are as follows:

$$a = \left(\frac{2}{r} - \frac{v^2}{G(m_\star + m_{\text{BH}})} \right)^{-1} \quad (1)$$

Table 3: Evaluated values of the impact parameter for the full disruption of a star with uniform density, $\tilde{b}_{\text{FTDE}} = b_{\text{FTDE}}/\rho_{\text{conc}}$.

γ	b_{FTDE}	ρ_{conc}^{-1}	\tilde{b}_{FTDE}
4/3	0.50	0.26	1.92
5/3	1.08	0.55	1.96

Notes. The columns indicate the polytropic index γ , the impact parameter for full disruption b_{FTDE} , the inverse of the density concentration factor ρ_{conc}^{-1} and the aforementioned parameter \tilde{b}_{FTDE} . The b_{FTDE} values for polytropic stars are from Mainetti et al. (2017).

$$e = \left(1 - \frac{(\mathbf{r} \times \mathbf{v})^2}{G(m_\star + m_{\text{BH}})a}\right)^{0.5} \quad (2)$$

We determine the spin angular momentum \mathbf{L}_\star about the star’s CoM using the masses m_i , relative positions \mathbf{r}_i and velocities \mathbf{v}_i of the bound gas cells. In the cases of full disruption, we ignore the orbital and spin parameters.

The ‘final’ post-disruption mass, orbital, and spin parameters reported in the following section are the means and standard deviations of these quantities during the last ten snapshots of each simulation (the time between consecutive snapshots was chosen to be approximately equal to the initial dynamical timescale of the star). In the cases where a partially disrupted star returns on a second passage within the simulation time, we chose snapshots close to the apoapsis of the first passage for the parameter calculations.

4. Results

Figure 3 shows selected snapshots of our suite of simulations. It can be visually seen that the final outcomes (FTDE or PTDE) depend on all the parameters that we considered – the stellar mass m_\star , the core hydrogen fraction H_c , the BH mass m_{BH} , and the impact parameter b .

The following sections detail the quantitative results. It should be noted that, henceforth, initial star parameters are given the subscript \star (e.g. m_\star , L_\star), while the post-disruption remnant parameters are given the subscript \diamond (e.g. m_\diamond , L_\diamond). Table A.1 provides detailed initial and post-disruption parameters for our 58 simulations.

4.1. Effect of density concentration factor

Ryu et al. (2020b) showed that, in the case of SMBHs, the critical impact parameter for full disruption, b_{FTDE} , is inversely proportional to the density concentration factor $\rho_{\text{conc}} \equiv (\rho_c/\bar{\rho})^{1/3}$, where $\bar{\rho}$ and ρ_c are average and central stellar density respectively (see also Law-Smith et al. 2020). A larger value of ρ_{conc} represents a denser core with a puffier outer layer, and vice-versa. This indicates that a star with higher core density requires a smaller impact parameter to fully disrupt. Quantitatively, b_{FTDE} can be written as:

$$b_{\text{FTDE}} = \rho_{\text{conc}}^{-1} \tilde{b}_{\text{FTDE}} \quad (3)$$

Here, \tilde{b}_{FTDE} is the critical impact parameter for the full disruption of a hypothetical star with uniform density, i.e., $\rho_{\text{conc}} = 1$ (see also Equation 15 of Ryu et al. 2020b). Table 3 displays the values of b_{FTDE} of stars with polytropic indices γ (where $P \propto \rho^\gamma$)

4/3 and 5/3 as calculated by Mainetti et al. (2017). Shown also are the analytically computed ρ_{conc} for these polytropes, and the subsequently evaluated (using Equation 3) \tilde{b}_{FTDE} values. We also estimate \tilde{b}_{FTDE} to be 1.95 ± 0.20 from our suite of simulations by fitting the remnant masses for given initial stellar and BH masses (see the following section for details), and find the values of b_{FTDE} . Despite the significant difference in the masses of the black holes, our estimated values agree with those from Mainetti et al. (2017). Estimates of this factor calculated by Ryu et al. (2020b), Law-Smith et al. 2020 and Kiroğlu et al. (2023) all lie within the error range. Since the former two studies are on SMBHs and the latter is on IMBHs, we reiterate that \tilde{b}_{FTDE} is almost independent of the mass of the BH for a very large range of BH masses. The consensus between the previous works in spite of different numerical schemes (general relativistic grid-based hydrodynamics, adaptive-mesh refinement, and SPH respectively) and the current work strengthens this point. Therefore, we will use our computed value of $\tilde{b}_{\text{FTDE}} = 1.95 \pm 0.20$ for the fit functions in the following sections.

For completeness, Figure 4 (and Table 1) shows the trend ρ_{conc}^{-1} for MESA $1 M_\odot$ MS stars, with our three stellar models highlighted. We see that a more evolved star has a smaller ρ_{conc}^{-1} (harder to fully disrupt) compared to a less evolved star (easier to fully disrupt) and that this relation is close to linear as a function of stellar age t_\star . Figure 5 shows the averaged ρ_{conc}^{-1} values for a range of masses of MESA-generated MS stars ($0.1 M_\odot - 20.0 M_\odot$) of two metallicities – 0.02 (near-Solar) and 0.002 (sub-Solar). We see that higher mass MS stars have denser cores and puffier outer layers (hence lower ρ_{conc}^{-1} values, which plateau for stars of masses $\gtrsim 1 M_\odot$ at $\sim 1.6-2.0$), while the opposite is true for lower mass MS stars. Moreover, metallicity affects ρ_{conc}^{-1} only slightly, with the metal-poor stars being slightly less (more) centrally concentrated when $m_\star > 1.0 M_\odot$ ($m_\star \leq 1.0 M_\odot$). The (approximate) values of ρ_{conc}^{-1} are crucial to applying our fits (see the following sections).

4.2. Post-disruption stellar and BH masses

After a disruption event, a star loses mass, some of which gets bound to (and eventually accreted onto) the BH while the rest of it becomes unbound from the system. Evidently, the closer the approach of the star is to the BH, the larger the mass lost from the star.

Figure 6 shows this trend for the case of a $1 M_\odot$ (left) and a $0.5 M_\odot$ (right) star that is disrupted by a $10 M_\odot$ (top) and a $40 M_\odot$ (bottom) BH. The post-disruption fractional mass loss $\Delta m_\star/m_\star$, where Δm_\star is the difference between the star’s initial mass m_\star and the remnant mass m_\diamond . It decreases almost exponentially with the impact parameter b . Moreover, a more evolved MS star loses less mass compared to a less evolved star for the same value of b . This is because a more evolved star, with a higher central concentration, requires a stronger tidal force (or smaller b) to strip the same amount of mass when compared to a less evolved star. Consequently, b_{FTDE} , corresponding to $\Delta m_\diamond/m_\star = 1$, is also lower for more evolved stars.

Furthermore, we see that roughly half the mass lost from the star stays bound to the BH, although this is not always true, especially when there is little mass loss (see Table A.1). This bound mass decreases through time due to continuous debris interaction resulting in mass unbinding, and hence is an upper limit for the mass that can be accreted onto the BH. Details of the accretion process and feedback from the BH might prevent some of the mass bound to the BH from being accreted, but following

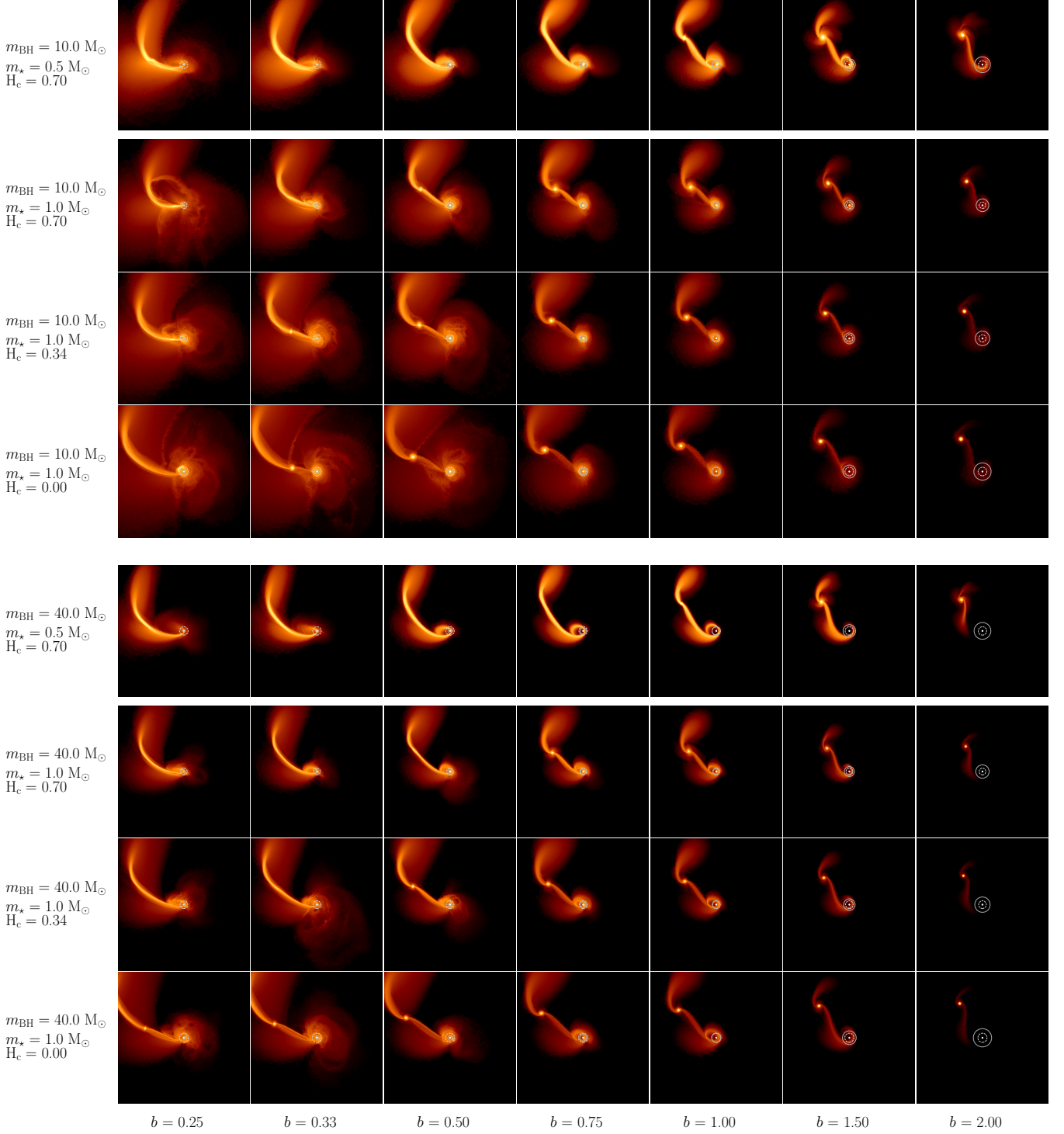


Fig. 3: Grid of log density slices of stars $\sim 20 t_{\text{dyn},\star}$ after undergoing μ TDEs, with the BH at the center of each panel. Each row is for a different m_{BH} (top and bottom half for $10 M_{\odot}$ and $40 M_{\odot}$ respectively), m_{\star} or H_c , whereas the columns represent increasing b (from left to right). The dashed and solid circles around the BH, most visible in the rightmost panels, denote the tidal radius, r_t , and the periapsis distance, r_p , respectively. Note that the spatial range of each panel is not the same.

this process is beyond the scope of our paper. The other half of the stripped mass is unbound from the BH-star system.

We can fit (with standard 1σ errors) the fractional mass loss Δm_{\star} well by:

$$\log_{10} \left(\frac{\Delta m_{\odot}}{m_{\star}} \right) = \min \{ (-2.10 \pm 0.10) (b - b_{\text{FTDE}}), 0 \} \quad (4)$$

Here, b_{FTDE} is as given in Equation 3. Since ρ_{conc} is taken into account, this fit differs from those obtained by Guillochon & Ramirez-Ruiz (2013) and Ryu et al. (2020c) for TDEs due to SMBHs. The remnant mass fit function does not explicitly depend on m_{\star} and m_{BH} , but only on b and ρ_{conc} . Since ρ_{conc} is higher for more evolved stars, they have a smaller b_{FTDE} and

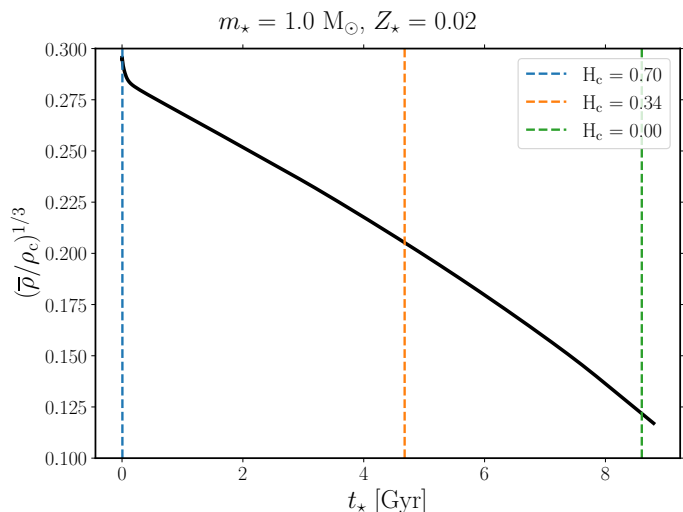


Fig. 4: MESA-derived inverses of density concentration factors ρ_{conc}^{-1} for a $1 M_{\odot}$ MS star as a function of stellar age. The three dashed vertical lines represent the ages of three chosen MS models in our study, corresponding to the profiles in Figure 1 and the values in Table 1. The dependence with age is very close to linear.

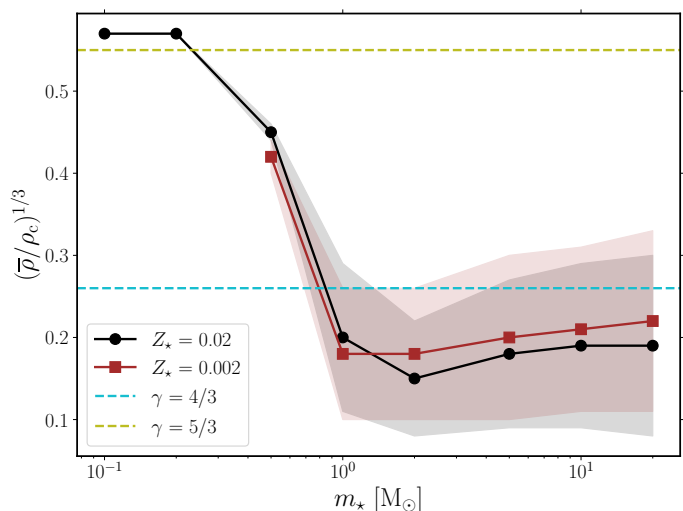


Fig. 5: MESA-derived inverses of density mean concentration factors ρ_{conc}^{-1} for MS stars of a range of masses (0.1, 0.2, 0.5, 1.0, 2.0, 5.0, 10.0 and 20.0 in units of M_{\odot}) and two metallicities – 0.02 and 0.002. The shaded regions illustrate the variation in ρ_{conc}^{-1} over the MS lifetime, with a TAMS star having the lowest ρ_{conc}^{-1} value and a ZAMS star having the highest (the values are for ZAMS stars only in the cases of stars of masses $< 1 M_{\odot}$). The two dashed horizontal lines represent the corresponding values for polytropic stars, shown in Table 3.

hence, less fractional mass loss. Figure 6 plots these best-fit curves, with the error bars shaded. It should be noted that this trend may not hold for larger values of b .

4.3. Post-disruption stellar spins

An initially non-rotating star gains spin after a tidal encounter due to tidal torques from the BH. Although we do not delve into the details of the spin-up, this results in *differential*, and

not rigid, rotation of the star. It should be noted that, due to spurious motions in our initial AREPO stellar models, the spin angular momenta L_{\star} are not zero but $\sim 1-2 \times 10^{47} \text{ g cm}^2 \text{ s}^{-1}$ ($\sim 2 \times 10^{46} \text{ g cm}^2 \text{ s}^{-1}$) for $1 M_{\odot}$ ($0.5 M_{\odot}$) stars. Since these values correspond to negligible equatorial surface velocities² of $\sim 10 \text{ m s}^{-1}$, the stars are considered to be non-rotating. The spin angular momentum of the remnant L_{\odot} depends on the internal structure of the original star and the impact parameter.

Figure 7 shows the trend of L_{\odot} with respect to the impact parameter b for the case of a $1 M_{\odot}$ (left) and a $0.5 M_{\odot}$ (right) star being *partially* disrupted by a $10 M_{\odot}$ (top) and a $40 M_{\odot}$ (bottom) BH. In addition, we indicate the approximate, order-of-magnitude estimates of the break-up angular momenta (assuming uniform density and rigid rotation) of the remnant stars, $L_{\odot, \text{break}} = 0.4 m_{\odot} r_{\odot} v_{\odot, \text{break}}$ ³. Here, we crudely estimate the remnant radius as $(r_{\odot}/R_{\odot}) = (m_{\odot}/M_{\odot})^{0.7}$ and assume the break-up velocity to be the Keplerian velocity at r_{\star} , i.e., $v_{\odot, \text{break}} = \sqrt{Gm_{\odot}/r_{\odot}}$. In reality, the remnant is significantly puffed up, and the break-up velocity would depend on the true moment of inertia of the remnant (and thus, its density profile) and the differential rotation due to spin-up. For our range of simulation parameters, L_{\odot} remains below $L_{\odot, \text{break}}$, although significant mass loss can bring the remnant very close to break-up, e.g., $m_{\star} = 0.5 M_{\odot}$ and $b \lesssim 1.00$. For higher values of b (but still less than $b \sim 2$), L_{\odot} decreases almost exponentially as b increases. On the other hand, when b is less such that a fractional mass loss is $\geq 2 \times 10^{-1}$, the trend reverses until FTDE. This trend reflects the counter-balance between mass loss and spin-up: for stronger PTDEs, although the remnant is spun up more rapidly, the remnant mass is smaller.

The large spin-up for smaller b indicates that the specific angular momentum monotonically increases as b decreases. Motivated by this, we considered the *scaled* (moment of inertia-adjusted) parameter $L_{\odot, \text{scaled}} \equiv L_{\odot}/(m_{\odot, \text{frac}} \tilde{r}_{\odot, \text{frac}}^2)$. Here, the fractional remnant mass $m_{\odot, \text{frac}} \equiv m_{\odot}/m_{\star}$ and the post-disruption estimated fractional radius $\tilde{r}_{\odot, \text{frac}}/R_{\odot} = m_{\odot, \text{frac}}^{0.7}$ is a crude estimate of the radius of an MS star.

We found the following exponential fit (with standard 1σ errors) describes $L_{\odot, \text{scaled}}$ well:

$$\log_{10} \left(\frac{L_{\odot, \text{scaled}}}{\text{g cm}^2 \text{ s}^{-1}} \right) = (-1.50 \pm 0.15) b + (52.00 \pm 0.30) \quad (5)$$

From the definition of $\tilde{r}_{\star, \text{frac}}$ before, we have:

$$L_{\odot} = L_{\odot, \text{scaled}} \left(\frac{m_{\odot}}{m_{\star}} \right)^{2.4} = L_{\odot, \text{scaled}} \left(1 - \frac{\Delta m_{\odot}}{m_{\star}} \right)^{2.4} \quad (6)$$

Here, $(\Delta m_{\odot}/m_{\star})$ is estimated using Equation 4. This equation implies that the post-disruption spin depends significantly on the fractional mass loss. Moreover, there is no dependence on m_{BH} . Figure 7 plots these best-fit curves, with the error bars shaded.

4.4. Post-disruption orbital parameters

Depending on the stellar structure and the BH mass, a star in an initially parabolic orbit ends up in an eccentric or even a hyperbolic orbit after a PTDE (see also Ryu et al. 2020c; Kremer et al. 2022; Kiroğlu et al. 2023). The specific orbital energy of

² In contrast, the Sun, a very slow rotator, has an equatorial surface velocity of $\sim 2 \text{ km s}^{-1}$.

³ This is because hypothetical star (sphere) of uniform density has a moment of inertia of $I_{\star, \text{uniform}} = 0.4 m_{\star} r_{\star}^2$ about an axis of rotation passing through the center.

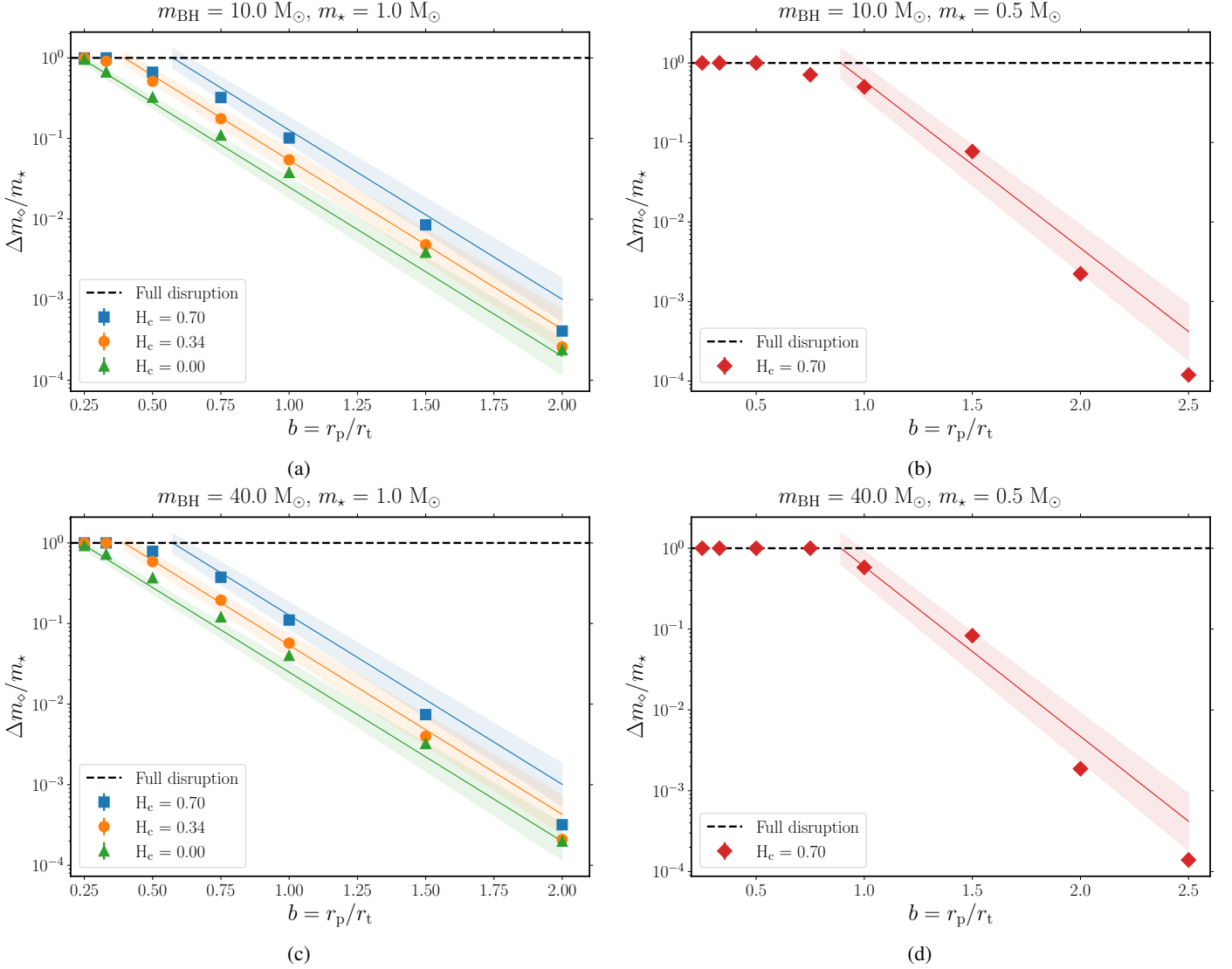


Fig. 6: Post-disruption fractional mass loss, $\Delta m_{\odot}/m_{\star}$, for a star of mass $1 M_{\odot}$ (left) and $0.5 M_{\odot}$ (right), due to a BH of mass $10 M_{\odot}$ (top) and $40 M_{\odot}$ (bottom), as a function of impact parameter b and MS age (H_c abundance). The dashed line at the top signifies the full disruption of the star. The fractional mass losses are largely independent of BH mass. Mass loss is higher for lower b values, and this decreases roughly exponentially (best-fit lines and standard error regions shown) with increasing b . A less evolved star (higher H_c) loses more mass for the same value of b . A $0.5 M_{\odot}$ star has a higher mass loss than a $1 M_{\odot}$ star for the same b .

the star-BH system, ε_{orb} , is the sum of the specific energy injected into stellar tides, $\varepsilon_{\text{tide}}$, the specific binding energy of the ejected material, $\varepsilon_{\text{bind}}$, and the specific ‘kick’ energy, $\varepsilon_{\text{kick}}$ (see Kremer et al. 2022). Manukian et al. (2013) estimated the potentially unbinding ‘kick’ received by a star undergoing PTDE due to an SMBH from asymmetric mass loss and observed that it depends solely on the mass loss and not on the star-SMBH mass ratio. However, this is not true for μ TDEs – the mass ratio determines the kick, and hence the boundedness, of the star-SBH system (see also Figure 2 of Kiroğlu et al. 2023 for TDEs due to IMBHs).

Figure 8 shows the post-disruption specific orbital energy of the star-BH system, ε_{orb} , for the disruption of a $1 M_{\odot}$ and a $0.5 M_{\odot}$ star by a $10 M_{\odot}$ (top panel) and a $40 M_{\odot}$ (bottom panel) BH. The values are normalized to the square of $\sigma = 10 \text{ km s}^{-1}$, the typical velocity dispersion of Milky Way globular clusters (e.g., Baumgardt & Hilker 2018). More negative (positive) values represent more bound (unbound) orbits. In general, ε_{orb} be-

comes more negative with decreasing b . If the density concentration factor ρ_{conc} is high enough (as in the case of a TAMS $1 M_{\odot}$ star; see Figure 4), this trend continues till FTDE. However, in the case of a ZAMS $1 M_{\odot}$ star (and less extremely in a MAMS star), there is a certain value of b at which ε_{orb} starts to increase with decreasing b . This is due to the momentum kick from asymmetric mass loss, which becomes significant when the mass loss is high. In the case of a PTDE of a $1 M_{\odot}$ ZAMS star by a $40 M_{\odot}$ BH, the post-disruption orbit can be hyperbolic (unbound) for b values close to FTDE. This trend is more extreme for a $0.5 M_{\odot}$ star, with hyperbolic orbits being possible even in the case of PTDE by a $10 M_{\odot}$ BH. Moreover, their velocities at infinity are high enough ($\sim 100\text{--}300 \text{ km s}^{-1}$) to escape the cluster entirely. The two different BH masses result in quite different quantitative orbital parameters. Similar to Kremer et al. 2022, we can write each of the energy components as follows:

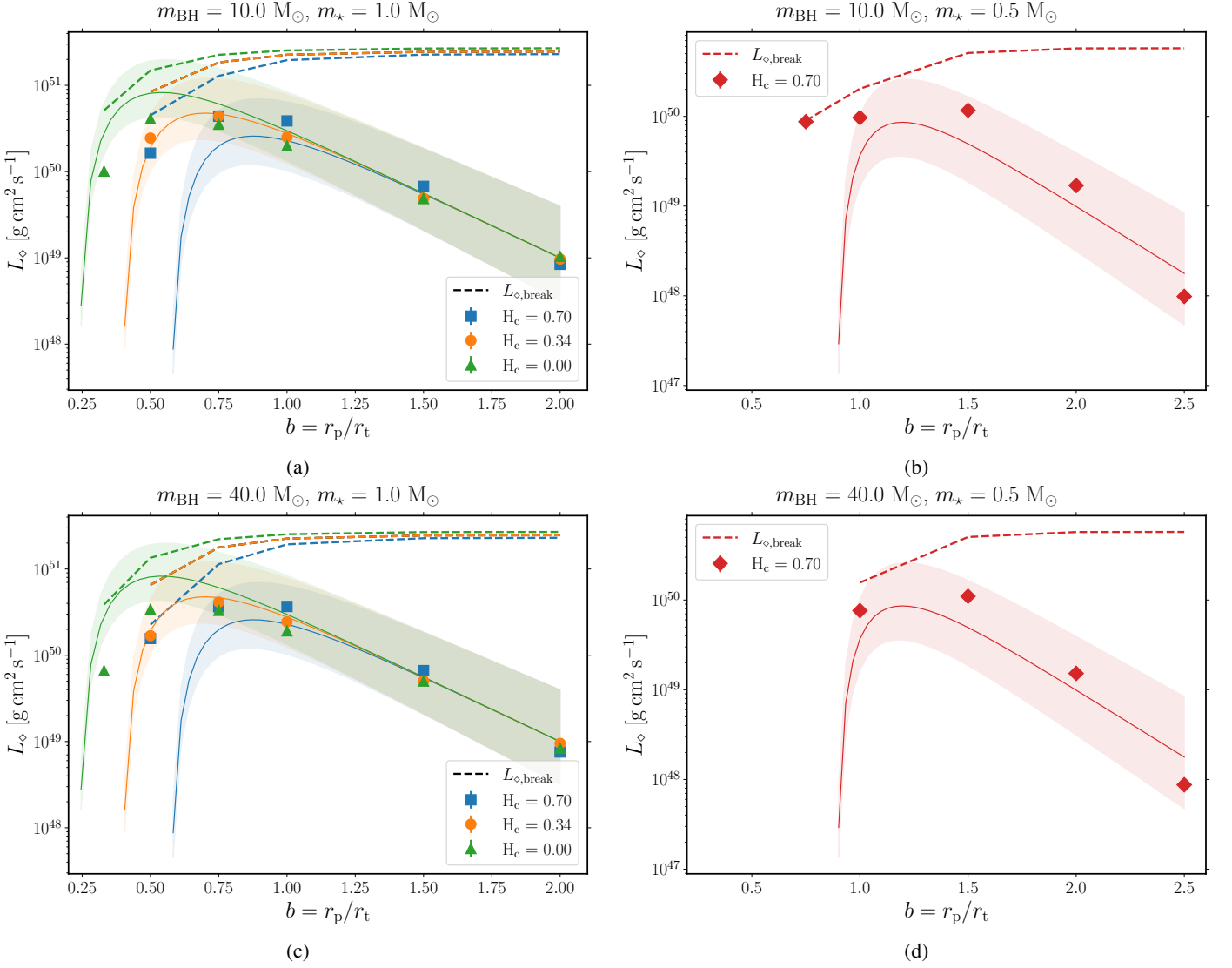


Fig. 7: Post-disruption spin angular momentum, L_∞ , for an initially non-rotating star of mass $1 M_\odot$ (left) and $0.5 M_\odot$ (right), due to a BH of mass $10 M_\odot$ (top) and $40 M_\odot$ (bottom), as a function of impact parameter b and MS age (H_c abundance). The dashed lines indicate the (approximate) estimated break-up angular momenta of the remnants $L_{\infty,\text{break}}$ respectively. The spin angular momenta are largely independent of BH mass. It decreases almost exponentially for sufficiently high b values, and it drops for very low b values when the remnant mass is small (best-fit lines and standard error regions shown). The drop-off of angular momentum occurs at larger b for a less evolved star.

$$\varepsilon_{\text{tide}} = -\frac{Gm_{\text{BH}}^2}{r_\star m_\odot} \left[\left(\frac{r_\star}{r_p} \right)^6 T_2 + \left(\frac{r_\star}{r_p} \right)^8 T_3 \right] \quad (7)$$

$$\varepsilon_{\text{bind}} = -\frac{G\Delta m_\odot}{2r_\star} \quad (8)$$

$$\varepsilon_{\text{kick}} = \frac{Gm_{\text{BH}}\Delta m_\odot r_\star^2}{r_p^3 m_\odot} \quad (9)$$

Here, T_2 and T_3 are terms which depend on the stellar mass, radius, and density structure, BH mass, and distance of approach (Press & Teukolsky 1977; Lee & Ostriker 1986). For the range of parameters considered, with $m_{\text{BH}} > m_\star$ and $r_p \sim r_\star$, the values of T_2 and T_3 lie in the range $0.01 - 0.1$. These values are systematically lower for stars with lower ρ_{conc} values. As a result, in $0.5 M_\odot$ stars (and ZAMS $1 M_\odot$ stars), $\varepsilon_{\text{tide}}$ is dominated by $\varepsilon_{\text{kick}}$, resulting in them becoming unbound from the BH. It

should be noted that $\varepsilon_{\text{tide}}$ depends very strongly on the distance of approach.

In addition, we find that the change in the specific orbital angular momentum of the star-BH system, h_{orb} , is not significant. For orbits very close to being parabolic, which is the case for all our post-disruption orbits (see Figure 9), $h_{\text{orb}} \approx \sqrt{2G(m_\star + m_{\text{BH}})r_p} \approx \sqrt{2Gm_{\text{BH}}r_p}$. This implies that the post-disruption periastron distance $r_p = a(1 - e)$, where a is the semi-major axis and e is the eccentricity, is nearly the same as the initial periastron distance $r_p \equiv br_t$, which is also seen in PTDEs by SMBHs (Ryu et al. 2020c). Consequently, given that $a = -0.5G(m_\star + m_{\text{BH}})/\varepsilon_{\text{orb}}$, the calculation of e is straightforward. Figure 9 shows the post-disruption e , computed using Equations 1 and 2, as a function of b which follows the trend in ε_{orb} .

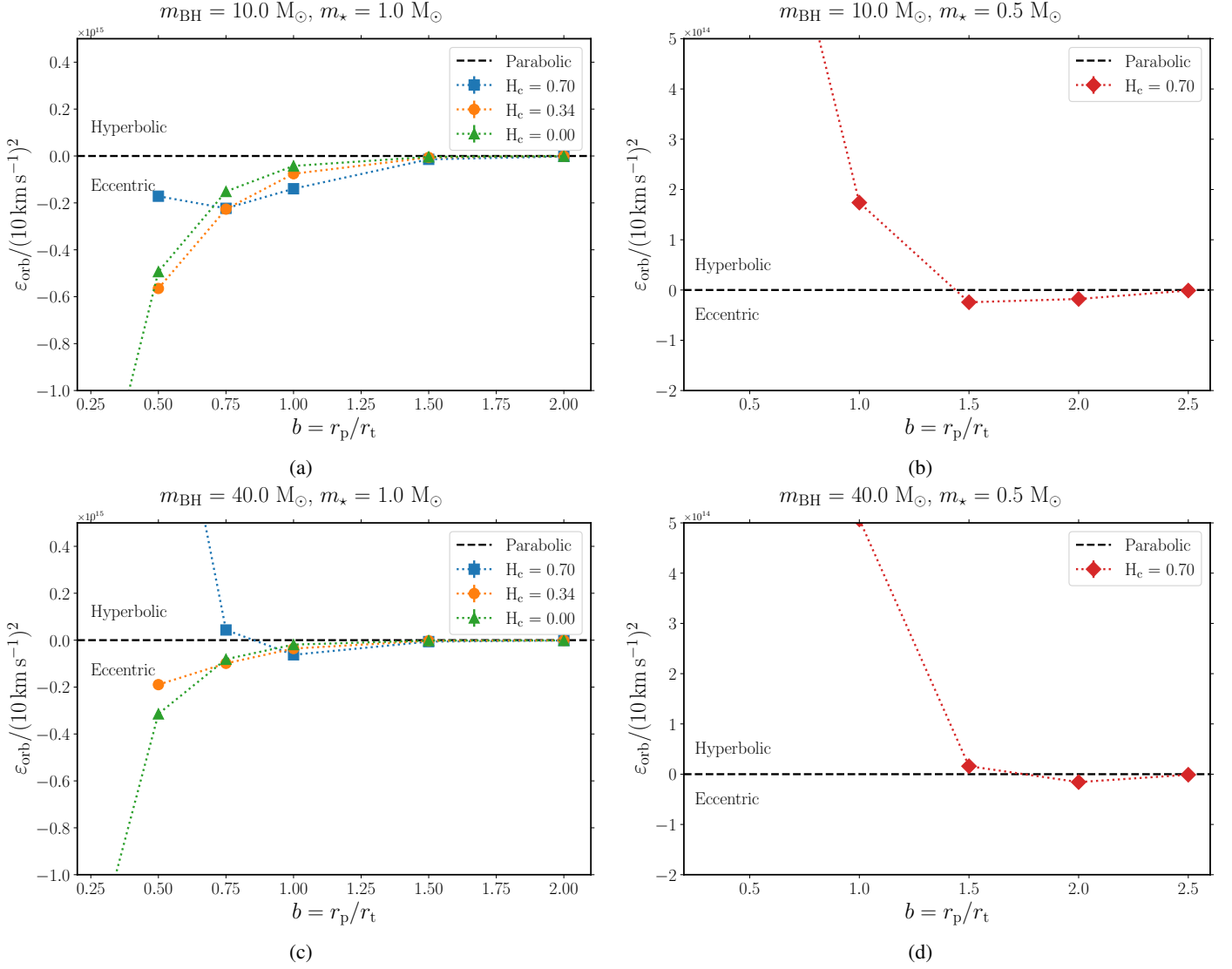


Fig. 8: Post-disruption normalized specific orbital energies of the star-BH system, ε_{orb} , for a star of mass $1 M_{\odot}$ (left) and $0.5 M_{\odot}$ (right) initially in a parabolic orbit, due to a BH of mass $10 M_{\odot}$ (top) and $40 M_{\odot}$ (bottom), as a function of impact parameter b and MS age (H_c abundance). The dashed line represents parabolic orbits and separates the parameter space into bound (eccentric) and unbound (hyperbolic) orbits. When mass loss is relatively low, a lower value of b generally results in more negative ε_{orb} in the case of $1 M_{\odot}$ star. This trend continues for the TAMS star. However, for the ZAMS and MAMS stars, significant mass losses can reverse this trend, with hyperbolic orbits also being a possibility (e.g., $1 M_{\odot}$ ZAMS star and $40 M_{\odot}$ BH mass with $b < 1.00$). $0.5 M_{\odot}$ stars, on the other hand, can become unbound for larger b , with boundedness also depending on the mass of the BH.

4.5. Rates of tidal encounters

The rate of μ TDEs per year per Milky Way-like galaxy (similar to Perets et al. 2016) can be expressed as:

$$R_{\mu\text{TDE}} \sim N_{\text{clus}} N_{\star,c} N_{\text{BH},c} \Sigma \sigma V_c^{-1} \quad (10)$$

Here, $N_{\text{clus}} \sim 150 \text{ MWGal}^{-1}$ is the number of globular clusters (in the Milky Way, e.g., Harris 2010), $N_{\star,c}$ is the number of stars in a cluster core, $N_{\text{BH},c}$ is the number of BHs in a cluster core, $\Sigma = \pi r_p^2 (1 + v_p^2/\sigma^2)$ is the gravitational focused encounter cross-section with periastris distance $r_p = br_t$ (see Section 2) and periastris velocity $v_p = \sqrt{G(m_{\text{BH}} + m_{\star})/r_p}$, and σ is the velocity dispersion of the cluster. For globular clusters in the Milky Way Galaxy, the typical values of these parameters are $n_{\star,c} = N_{\star,c} V_c^{-1} \sim 10^2\text{--}10^7 \text{ pc}^{-3}$ (e.g., Baumgardt & Hilker 2018), $N_{\text{BH},c} \sim 10\text{--}100$ (e.g., Morscher et al. 2015; Askar et al.

2018), $\sigma \sim 1\text{--}20 \text{ km s}^{-1}$ (e.g., Baumgardt & Hilker 2018). With these values, and assuming $v_p \gg \sigma$ in globular clusters, and typical star and BH masses of $1 M_{\odot}$ and $10 M_{\odot}$ respectively, the rate is:

$$R_{\mu\text{TDE}} \sim 10^{-6} \text{ yr}^{-1} \text{ MWGal}^{-1} \left(\frac{N_{\text{clus}}}{150 \text{ MWGal}^{-1}} \right) \left(\frac{n_{\star,c}}{10^{-5} \text{ pc}^{-3}} \right) \left(\frac{N_{\text{BH},c}}{100} \right) \left(\frac{\sigma}{10 \text{ km s}^{-1}} \right) \left(\frac{m_{\text{BH}} + m_{\star}}{11 M_{\odot}} \right) \left(\frac{r_p/r_t}{1.0} \right) \quad (11)$$

This equation implies that PTDEs (with larger r_p/r_t) are more frequent than FTDEs. More specifically, from our simulations of TDEs of $1 M_{\odot}$ stars by $10 M_{\odot}$, encounters with $b \sim 1\text{--}2$ would result in eccentric bound orbits, which can circularize over time through tides. A more detailed rate calculation would involve integrating Equation 11 over a range of star and black hole masses.

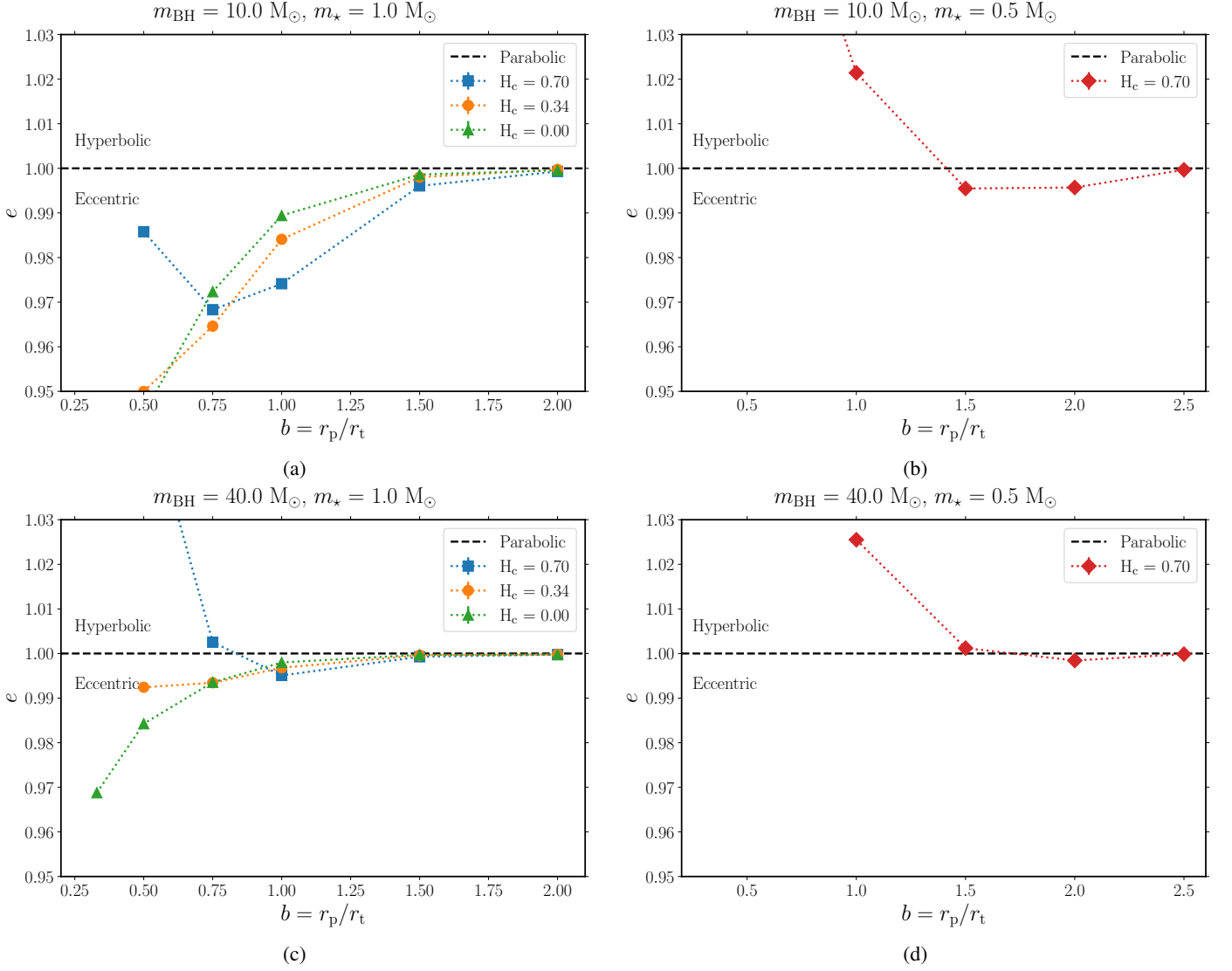


Fig. 9: Post-disruption orbital eccentricities, e , for a star of mass $1 M_{\odot}$ (left) and $0.5 M_{\odot}$ (right) initially in a parabolic orbit, due to a BH of mass $10 M_{\odot}$ (top) and $40 M_{\odot}$ (bottom), as a function of impact parameter b and MS age (H_c abundance). The dashed line represents parabolic orbits and separates the parameter space into bound (eccentric) and unbound (hyperbolic) orbits. The reasoning for the trends is the same as that for Figure 8.

The above rates are derived for μ TDEs produced in dense stellar systems such as globular clusters and nuclear star clusters. However, other channels also contribute to μ TDEs (see discussion in Perets et al. 2016), such as ultra-wide binaries and triples in the field (Michaely & Perets 2016, 2020) and post-natal-kicks leading to close encounter between a newly formed BH and a stellar companion (Michaely et al. 2016). These channels may give rise μ TDEs in young environments and in the field.

4.6. Summary of fits

Below we present the post-disruption fits detailed in previous sections for use in globular cluster codes. $m_{\star \rightarrow \text{BH}}$ refers to the gas mass bound to the black hole after disruption, including the accreted mass.

4.6.1. Masses of remnant star and BH

$$\left(\frac{\Delta m_{\odot}}{m_{\star}}\right) = 10^{\min\{-2.10(b-1.95\rho_{\text{conc}}^{-1}), 0\}} \quad (12)$$

$$\left(\frac{m_{\star \rightarrow \text{BH}}}{m_{\star}}\right) \leq 0.5 \left(\frac{\Delta m_{\odot}}{m_{\star}}\right) \quad (13)$$

4.6.2. Spin of remnant star

$$\left(\frac{L_{\odot}}{\text{g cm}^2 \text{ s}^{-1}}\right) = 10^{(-1.50b+52.00)} \left(\frac{m_{\star}}{M_{\odot}}\right)^{-1} \left(1 - \frac{\Delta m_{\odot}}{m_{\star}}\right)^{2.4} \quad (14)$$

4.6.3. Validity of fits

It should be noted that the density concentration factor, ρ_{conc} , only captures the full disruption of a star. Similarly defined factors for each radius r , i.e. $(\rho(r)/\bar{\rho})^{1/3}$, are required to calculate the distance at which mass beyond r is lost (see Ryu et al. 2020b).

Stars of higher masses tend to have much steeper density profiles when compared to $1 M_{\odot}$ stars, thus Equation 4, which fits the mass loss, is not universal. In particular, the mass loss fit for $2 M_{\odot}$ stars would involve an exponent of ~ 3 , unlike our derived exponent of ~ 2.1 in Equation 4. Similar arguments follow for the fits of spins and orbits.

5. Implications

In this section, we discuss the general observational implications and the caveats of our study. μ TDEs can potentially produce both unique and peculiar transient events as well as longer-lived systems.

5.1. Low-mass X-ray binaries

Low-mass X-ray binaries (LMXBs) are interacting binary systems which consist of compact objects (neutrons stars or black holes) accreting mass from their low-mass ($\lesssim 1 M_{\odot}$) stellar companions, thereby producing X-rays. A few hundred of LMXBs have been detected in the Milky Way Galaxy (e.g., Liu et al. 2007; Avakyan et al. 2023), highlighting the prevalence of such systems. However, theoretical (e.g., Portegies Zwart et al. 1997; Kalogera 1999) and population synthesis (e.g., Podsiadlowski et al. 2003; Kiel & Hurley 2006) studies have not been able to match the rates of observed LMBXs through isolated binary evolution alone. The primary reason is that a low-mass companion has insufficient energy to expel a common envelope during the giant phase of the primary star, thereby resulting in the spiraling in of the companion and an eventual merger. Thus, a dynamical channel formation channel for LMXBs, where a low-mass star is tidally captured by a black hole in a globular/nuclear cluster, holds promise (e.g., Voss & Gilfanov 2007; Michaely & Perets 2016; Klencki et al. 2017).

Some of our simulations of encounters of low-mass stars with black holes are not close enough for significant mass loss and can result in highly eccentric bound orbits. For example, in the parabolic encounter of a $1 M_{\odot}$ star and a $10 M_{\odot}$ BH, for $b \sim 1.0$ – 1.5 (see Section 4), the fractional mass loss is ~ 1 – 10% , and the post-disruption bound orbit has a period of 0.1 – 1 yr and an eccentricity of ~ 0.97 – 0.98 . However, tidal dissipation at subsequent periastris passages can reduce the eccentricity and orbital period (e.g., Klencki et al. 2017) such that the resulting bound system evolves into a compact LMXB.

Another type of system that is potentially formed through dynamical encounters are non-interacting BH-star systems, e.g., El-Badry et al. (2023a,b); Chakrabarti et al. (2023). These systems consist of $\sim 1 M_{\odot}$ stars orbiting $\sim 10 M_{\odot}$ black holes in moderately-eccentric orbits with periods of ~ 1 yr. These parameters correspond quite well with our simulations with $b \sim 1.0$ – 1.5 , which lends credence to dynamical formation.

5.2. Intermediate-mass black hole growth

Intermediate-mass black holes (IMBHs; see Greene et al. 2020 for a review), with masses greater than those of stellar-mass black holes ($\gtrsim 10^2 M_{\odot}$) and less than those of supermassive black holes ($\lesssim 10^6 M_{\odot}$), are expected to exist in the centers of dwarf galaxies (e.g., Kunth et al. 1987; Filippenko & Sargent 1989; Reines 2022; Gültekin et al. 2022) and globular clusters (e.g., Davis et al. 2011; Farrell et al. 2014; Pechetti et al. 2022). Among several IMBH formation mechanisms (see Volonteri et al. 2021 for review), one possible avenue is runaway mass

growth through tidal capture and disruption, which has been examined analytically (e.g., Stone et al. 2017) and numerically (e.g., Rizzuto et al. 2023; Arca Sedda et al. 2023). One of the most critical factors in this mechanism for BH growth is the amount of debris mass that ultimately accretes onto the BH. For example, Rizzuto et al. (2023) assume that a star approaching a BH within the nominal tidal radius r_t is fully destroyed and 50% of the stellar mass is accreted onto the BH.

While these assumptions may be valid for a part of the parameter space, it is important to develop a prescription for the outcomes of TDEs that works over a broader parameter range to more accurately assess the possibility of BH mass growth through TDEs. Our simulations can provide such prescriptions that can improve the treatment of TDEs. Firstly, our simulations show, like previous work on TDEs by supermassive black holes (e.g., Guillochon & Ramirez-Ruiz 2013; Mainetti et al. 2017; Goicovic et al. 2019; Ryu et al. 2020a,b,c,d; Law-Smith et al. 2020), that the periastris distances at which stars are fully or partially destroyed depend on the stellar internal structure. Ryu et al. (2020b) analytically demonstrated that the nominal tidal radius r_t is a more relevant quantity for partial disruption events involving stars with $m_{\star} \gtrsim 1 M_{\odot}$. Only for lower-mass stars, where $\rho_{\text{conc}} \sim 1$, does r_t come close to the genuine full disruption radius⁴. Our fitting formula for the fractional mass loss, Equation 4, can provide a better prescription for determining the fate of the star (full or partial disruption) as well as the mass of the remnant.

The amount of debris accreted onto the BH remains highly uncertain. To the zeroth order, if the accretion rate is super-Eddington, the strong radiation pressure gradient would drive strong outflows, hindering continuous and steady accretion (Sądowski et al. 2014). However, the accretion efficiency would be collectively affected by many factors, including magnetic fields, black hole spins, accretion flow structure, and jet formation (e.g., Sądowski et al. 2014; Jiang et al. 2019; Curd & Narayan 2023; Kaaz et al. 2023). Our fitting formulae for the fractional mass loss cannot provide an accurate prescription for the accreted mass but can place constraints on the maximum mass that can be accreted onto the BH.

5.3. Fast blue optical transients

Fast blue optical transients (FBOTs) are a class of optical transients characterized by high peak luminosities $> 10^{43}$ erg s⁻¹, rapid rise and decay times of the order of a few days, blue colors (Perets et al. 2011; Drout et al. 2014), and peak black-body temperatures of a few 10^4 K. Although a majority of these events can be explained by supernovae with low-mass ejecta (Pursiainen et al. 2018), a ‘luminous’ subset, e.g., AT2018cow (‘the Cow’; Smartt et al. 2018; Prentice et al. 2018), AT2018lqh (Ofek et al. 2021), AT2020mrf (Yao et al. 2022), CSS161010 (Coppejans et al. 2020), ZTF18abvkwla (‘the Koala’; Ho et al. 2020), AT2020xnd (‘the Camel’; Perley et al. 2021), AT2022tsd (‘the Tasmanian Devil’; Matthews et al. 2023), AT2023fhn (‘the Finch’; Chrimes et al. 2024), are too bright at their peaks and fade too rapidly to be explained by supernovae. Proposed mechanisms involve compact objects, such as black hole accretion or magnetars formed in core-collapse supernovae (Prentice et al. 2018), mergers between Wolf-Rayet stars and compact objects accompanied by hyper-accretion (Metzger 2022), or tidal dis-

⁴ The genuine full disruption radius and the partial disruption radius are proportional to $\rho_c^{-1/3}$ and $\bar{\rho}^{-1/3}$ respectively (see Section 4 of (Ryu et al. 2020b)).

ruption events by intermediate-mass BHs (Kuin et al. 2019) or stellar-mass BHs (Kremer et al. 2021).

Some luminous FBOTs also emit in radio or X-ray (e.g., Margutti et al. 2019; Ho et al. 2020) which indicates the presence of a circumstellar medium that may result from partial TDEs (Kremer et al. 2021). Our simulations support this notion by showing the presence of debris near the BH with occasional weak outflows from the BH. In addition, the remnants in our simulations are often bound to the BH and can subsequently undergo multiple partial disruptions, e.g., our simulations of TAMS $1 M_{\odot}$ stars and $10 M_{\odot}$ BHs for $b = 0.25$ or $b = 0.33$. While we cannot confirm a direct correlation between FBOTs and μ TDEs, multiple disruption events of a star may fulfill some of the astrophysical conditions (e.g., the presence of a gas medium and rapid accretion onto a compact object) necessary to explain FBOTs with radio emission. For such cases, the detection of repeated bursts in FBOTs could provide valuable constraints on their formation mechanisms.

5.4. Ultra-long gamma-ray bursts and X-ray flares

The exact appearance of transients resulting from μ TDEs is highly uncertain and depends on various assumptions. Perets et al. (2016) suggested that, if the accretion onto the BH is efficient and gives rise to jets, there is a possibility of producing ultra-long gamma-ray bursts (GRBs) and/or X-ray flares (XRFs).

Assuming a proportional relation between the material accreted to the compact object and the luminosity produced by the jet, we can generally divide μ TDEs into two regimes: (1) $t_{\min} \gg t_{\text{acc}}$ and (2) $t_{\min} \ll t_{\text{acc}}$, where t_{\min} is the typical fallback time of the debris following the disruption, and t_{acc} is the typical viscous time of the accretion disk that can form around the BH (see Perets et al. 2016 for more details).

- $t_{\min} \gg t_{\text{acc}}$: When the mass of the star is much smaller than that of the BH, the accretion evolution is dominated by the fallback rate, i.e., the light curve should generally follow the regular power-law (e.g. $t^{-5/3}$ power-law for a full disruption).
- $t_{\min} \ll t_{\text{acc}}$: When the masses of the star and the BH are comparable, the fallback material is expected to accumulate and form a disk on the fallback time, which then drains on the longer viscous time maintaining a low accretion rate. We would expect the flaring to begin only once the material is accreted onto the compact object. Therefore, we expect four stages in the light curve evolution: (1) A fast rise of the accretion flare once the disk material is processed and evolves to accrete on the compact object. (2) Accretion from the disk until the accumulated early fallback material is drained; if we assume a steady state accretion until drainage, one might expect a relatively flat light curve. (3) Once the disk drains the accumulated early fall-back material the light curve should drop steeply. (4) The continuous fall-back of material would govern the accretion rate at times longer than the viscous time, and the accretion rate should then follow the $t^{-5/3}$ rate (or a different power-law). The exact light curve at the early stages is difficult to predict, but we do note a non-trivial signature of the μ TDEs relating to the early and late stages.

The expected properties of μ TDEs are consistent with and might explain the origins of ultra-long GRBs (Levan et al. 2014): long-lived ($\sim 10^4$ s) GRBs which show an initial plateau followed by a rapid decay. μ TDEs may also explain the origin of some Swift TDE candidates (Bloom et al. 2011; Burrows et al. 2011; Cenko et al. 2012; Brown et al. 2015), suggested to be

produced through a TDE by a supermassive BH. The typical timescales for the latter are longer than the observed 10^5 s, challenging the currently suggested origin, but quite consistent with a μ TDE scenario.

μ TDEs producing ultra-long GRBs are also expected to produce afterglow emission if/when the strong outflows and jets launched by accretion propagate into the surrounding medium and the resulting shock interaction produces high energy particles which give rise to synchrotron and inverse Compton radiation. Such observational signature of μ TDE has been little explored, though analogous observation and modeling have been suggested for TDEs by massive black holes (e.g., Giannios & Metzger 2011; Zauderer et al. 2011). Detection of afterglows from μ TDEs would provide information on the energetics and dynamics of the outflow, robust independent evidence for the jet collimation, as well as identification of the host galaxy.

5.5. Remnants

Partial μ TDEs of stars by stellar BHs can spin up the stars significantly due to strong tidal interactions (see Fig. 7 and Alexander & Kumar 2001). Though magnetic breaking can potentially spin down such stars over time, observations of highly spun-up low-mass old stars in globular clusters could provide potential signatures for partial μ TDEs. In addition, the remnant undergoes violent chemical mixing during the first pericenter passage and has higher entropy than an ordinary star of the same mass and age (Ryu et al. 2020c, 2023a). If the mass loss is significant, a unique chemical composition profile may persist even after the remnant has relaxed to a stable state. This suggests that the remnant could exhibit unique asteroseismic signatures that distinguish it from ordinary stars (Bellinger et al. 2023, in prep).

5.6. Caveats

As mentioned in Section 2, we exclude the effects of relativity and magnetic fields in our study. The Newtonian approximation is justified for TDEs by SBHs because most of the debris stays outside r_p , which is approximately four orders of magnitude greater than the gravitational radius $r_g \equiv Gm_{\text{BH}}/c^2$ ⁵. However, relativistic effects and proper treatment of radiation are more important for the accretion flow, which is beyond the scope of our paper. The effect of magnetic fields on the dynamics of the remnant is unclear, which we will leave for our future work. A final point to note is that, unlike globular clusters, nuclear star clusters have typical velocity dispersions of $\sigma \gtrsim 100 \text{ km s}^{-1}$ (Figer et al. 2003; Schödel et al. 2009) depending on the galaxy, and subsequently, $|1 - e| \gtrsim 10^{-2}$. Thus, encounters are not always parabolic, and for a more thorough study, hyperbolic encounters must be taken into account.

6. Summary and conclusion

We performed a grid of 58 hydrodynamics simulations, using the moving-mesh code AREPO, of partial (PTDE) and full (FTDE) tidal disruptions of main-sequence (MS) stars with stellar-mass black holes (SBH) on initially-parabolic orbits. Our varied parameters include stellar mass m_{\star} ($0.5 M_{\odot}$ and $1.0 M_{\odot}$), SBH mass ($10 M_{\odot}$ and $40 M_{\odot}$), core hydrogen abundance H_c (a proxy for MS age t_{\star}) and impact parameter $b \equiv r_p/r_t$. Our stellar models are initialized in accordance with 1D detailed non-rotating

⁵ On the other hand, for TDEs with SMBHs, r_g and r_t can be comparable in scale.

stellar profiles from MESA. We also define a star’s density concentration parameter $\rho_{\text{conc}} \equiv (\rho_c/\bar{\rho})^{1/3}$. Our main results are summarized below:

- The mass of a post-disruption stellar remnant m_\circ decreases with decreasing b . A higher ρ_{conc} (more centrally concentrated) results in a lesser mass loss for the same b . m_\circ depends only on b and ρ_{conc} , and not on m_{BH} . Roughly half of the disrupted mass remains bound to the black hole, while the other half is unbound from the system.
- The spin angular momentum of a stellar remnant L_\circ increases after periastris passage. For large b (when the mass loss is small), L_\circ increases with decreasing b , but this trend reverses for very small b (close to FTDE) due to significant mass loss. This reversal occurs for lower b when ρ_{conc} is higher. The final spin is also independent of m_{BH} . For low b values, the rotational velocities can be very close to break-up velocities.
- Unlike mass and spin, the orbit of the remnant star also depends on m_{BH} . For large b , eccentricity e and semimajor axis a decrease with decreasing b keeping a constant periastris distance, i.e., the remnant tends to be more ‘bound’. Depending on m_{BH} and ρ_{conc} , this no longer holds for approaches close to FTDE – e can increase and the remnant can become unbound. In general, a higher m_{BH}/m_\star ratio and a lower ρ_{conc} tend to be unbinding.
- We provide relatively simple and accurate fitting formulae for the masses and spins of the remnant stars. These analytical fits are listed in Section 4.6 for easy access.

We discussed the implications that μ TDEs can have on low-mass X-ray binary formation, intermediate-mass black hole formation, and transient searches. Given the limited range of stellar masses and ages that we covered in this work, we will extend our suite of simulations in the future to cover a wider parameter space, including massive stars. It is necessary to explore this regime to model stellar dynamics in dense stellar clusters.

Acknowledgements. The authors thank Thorsten Naab for useful discussions regarding star-black hole encounters in star clusters. PV acknowledges the computational resources provided by the Max Planck Institute for Astrophysics to carry out this research.

References

Abbott, R., Abbott, T. D., Abraham, S., et al. 2021, *ApJ*, 913, L7
 Abbott, R., Abbott, T. D., Acernese, F., et al. 2023, *Physical Review X*, 13, 011048
 Alexander, T. & Kumar, P. 2001, *ApJ*, 549, 948
 Arca Sedda, M., Kamlah, A. W. H., Spurzem, R., et al. 2023, *MNRAS*, 526, 429
 Askar, A., Arca Sedda, M., & Giersz, M. 2018, *MNRAS*, 478, 1844
 Avakyan, A., Neumann, M., Zainab, A., et al. 2023, *A&A*, 675, A199
 Bagla, J. S. 2002, *Journal of Astrophysics and Astronomy*, 23, 185
 Baumgardt, H. & Hilker, M. 2018, *MNRAS*, 478, 1520
 Bellinger, E., Ryu, T., & Spruit, H. 2023, (in prep)
 Bellm, E. C., Kulkarni, S. R., Graham, M. J., et al. 2019, *PASP*, 131, 018002
 Bloom, J. S., Giannios, D., Metzger, B. D., et al. 2011, *Science*, 333, 203
 Brown, G. C., Levan, A. J., Stanway, E. R., et al. 2015, *MNRAS*, 452, 4297
 Burmester, U. P., Ferrario, L., Pakmor, R., et al. 2023, *MNRAS*, 523, 527
 Burrows, D. N., Kennea, J. A., Ghisellini, G., et al. 2011, *Nature*, 476, 421
 Cenko, S. B., Krimm, H. A., Horesh, A., et al. 2012, *ApJ*, 753, 77
 Chakrabarti, S., Simon, J. D., Craig, P. A., et al. 2023, *AJ*, 166, 6
 Chambers, K. C., Magnier, E. A., Metcalfe, N., et al. 2016, arXiv e-prints, arXiv:1612.05560
 Chimes, A. A., Jonker, P. G., Levan, A. J., et al. 2024, *MNRAS*, 527, L47
 Coppejans, D. L., Margutti, R., Terreran, G., et al. 2020, *ApJ*, 895, L23
 Curd, B. & Narayan, R. 2023, *MNRAS*, 518, 3441
 Davis, S. W., Narayan, R., Zhu, Y., et al. 2011, *ApJ*, 734, 111
 De Angelis, F., Piotta, G., Cassisi, S., et al. 2005, *AJ*, 130, 116
 Drout, M. R., Chornock, R., Soderberg, A. M., et al. 2014, *ApJ*, 794, 23

El-Badry, K., Rix, H.-W., Cendes, Y., et al. 2023a, *MNRAS*, 521, 4323
 El-Badry, K., Rix, H.-W., Quataert, E., et al. 2023b, *MNRAS*, 518, 1057
 Farrell, S. A., Servillat, M., Gladstone, J. C., et al. 2014, *MNRAS*, 437, 1208
 Figer, D. F., Gilmore, D., Kim, S. S., et al. 2003, *ApJ*, 599, 1139
 Filippenko, A. V. & Sargent, W. L. W. 1989, *ApJ*, 342, L11
 Gallegos-Garcia, M., Law-Smith, J., & Ramirez-Ruiz, E. 2018, *ApJ*, 857, 109
 Gehrels, N., Chincarini, G., Giommi, P., et al. 2004, *ApJ*, 611, 1005
 Gezari, S. 2021, *ARA&A*, 59, 21
 Giannios, D. & Metzger, B. D. 2011, *MNRAS*, 416, 2102
 Glanz, H., Perets, H. B., & Pakmor, R. 2023, arXiv e-prints, arXiv:2309.03300
 Goicovic, F. G., Springel, V., Ohlmann, S. T., & Pakmor, R. 2019, *MNRAS*, 487, 981
 Golightly, E. C. A., Nixon, C. J., & Coughlin, E. R. 2019, *ApJ*, 882, L26
 Greene, J. E., Strader, J., & Ho, L. C. 2020, *ARA&A*, 58, 257
 Gronow, S., Collins, C. E., Sim, S. A., & Röpke, F. K. 2021, *A&A*, 649, A155
 Guillochon, J. & Ramirez-Ruiz, E. 2013, *ApJ*, 767, 25
 Gültekin, K., Nyland, K., Gray, N., et al. 2022, *MNRAS*, 516, 6123
 Harris, W. E. 2010, arXiv e-prints, arXiv:1012.3224
 Ho, A. Y. Q., Perley, D. A., Kulkarni, S. R., et al. 2020, *ApJ*, 895, 49
 Jansen, F., Lumb, D., Altieri, B., et al. 2001, *A&A*, 365, L1
 Jiang, Y.-F., Stone, J. M., & Davis, S. W. 2019, *ApJ*, 880, 67
 Kaaz, N., Murguia-Berthier, A., Chatterjee, K., Liska, M. T. P., & Tchekhovskoy, A. 2023, *ApJ*, 950, 31
 Kalogera, V. 1999, *ApJ*, 521, 723
 Kiel, P. D. & Hurley, J. R. 2006, *MNRAS*, 369, 1152
 Kiroğlu, F., Lombardi, J. C., Kremer, K., et al. 2023, *ApJ*, 948, 89
 Klencki, J., Wiktorowicz, G., Gładysz, W., & Belczynski, K. 2017, *MNRAS*, 469, 3088
 Kochanek, C. S., Shappee, B. J., Stanek, K. Z., et al. 2017, *PASP*, 129, 104502
 Kollmeier, J., Anderson, S. F., Blanc, G. A., et al. 2019, in *Bulletin of the American Astronomical Society*, Vol. 51, 274
 Kramer, M., Schneider, F. R. N., Ohlmann, S. T., et al. 2020, *A&A*, 642, A97
 Kremer, K., Lombardi, J. C., Lu, W., Piro, A. L., & Rasio, F. A. 2022, *ApJ*, 933, 203
 Kremer, K., Lu, W., Piro, A. L., et al. 2021, *ApJ*, 911, 104
 Kuin, N. P. M., Wu, K., Oates, S., et al. 2019, *MNRAS*, 487, 2505
 Kunth, D., Sargent, W. L. W., & Bothun, G. D. 1987, *AJ*, 93, 29
 Law, N. M., Kulkarni, S. R., Dekany, R. G., et al. 2009, *PASP*, 121, 1395
 Law-Smith, J., Guillochon, J., & Ramirez-Ruiz, E. 2019, *ApJ*, 882, L25
 Law-Smith, J. A. P., Coulter, D. A., Guillochon, J., Mockler, B., & Ramirez-Ruiz, E. 2020, *ApJ*, 905, 141
 Lee, H. M. & Ostriker, J. P. 1986, *ApJ*, 310, 176
 Levan, A. J., Tanvir, N. R., Starling, R. L. C., et al. 2014, *ApJ*, 781, 13
 Lioutas, G., Bauswein, A., Soutanis, T., et al. 2024, *MNRAS*, 528, 1906
 Liu, Q. Z., van Paradijs, J., & van den Heuvel, E. P. J. 2007, *A&A*, 469, 807
 Lopez, Martin, J., Batta, A., Ramirez-Ruiz, E., Martinez, I., & Samsing, J. 2019, *ApJ*, 877, 56
 Mainetti, D., Lupi, A., Campana, S., et al. 2017, *A&A*, 600, A124
 Manukian, H., Guillochon, J., Ramirez-Ruiz, E., & O’Leary, R. M. 2013, *ApJ*, 771, L28
 Margutti, R., Metzger, B. D., Chornock, R., et al. 2019, *ApJ*, 872, 18
 Marín-Franch, A., Aparicio, A., Piotta, G., et al. 2009, *ApJ*, 694, 1498
 Martin, D. C., Fanson, J., Schiminovich, D., et al. 2005, *ApJ*, 619, L1
 Matthews, D., Margutti, R., Metzger, B. D., et al. 2023, *Research Notes of the American Astronomical Society*, 7, 126
 Metzger, B. D. 2022, *ApJ*, 932, 84
 Michaely, E., Ginzburg, D., & Perets, H. B. 2016, arXiv e-prints, arXiv:1610.00593
 Michaely, E. & Perets, H. B. 2016, *MNRAS*, 458, 4188
 Michaely, E. & Perets, H. B. 2020, *MNRAS*, 498, 4924
 Morscher, M., Pattabiraman, B., Rodriguez, C., Rasio, F. A., & Umbreit, S. 2015, *ApJ*, 800, 9
 Ofek, E. O., Adams, S. M., Waxman, E., et al. 2021, *ApJ*, 922, 247
 Ohlmann, S. T., Röpke, F. K., Pakmor, R., & Springel, V. 2016a, *ApJ*, 816, L9
 Ohlmann, S. T., Röpke, F. K., Pakmor, R., & Springel, V. 2017, *A&A*, 599, A5
 Ohlmann, S. T., Röpke, F. K., Pakmor, R., Springel, V., & Müller, E. 2016b, *MNRAS*, 462, L121
 Ondratschek, P. A., Röpke, F. K., Schneider, F. R. N., et al. 2022, *A&A*, 660, L8
 Pakmor, R., Callan, F. P., Collins, C. E., et al. 2022, *MNRAS*, 517, 5260
 Pakmor, R., Kromer, M., Taubenberger, S., & Springel, V. 2013, *ApJ*, 770, L8
 Pakmor, R., Springel, V., Bauer, A., et al. 2016, *MNRAS*, 455, 1134
 Pakmor, R., Zenati, Y., Perets, H. B., & Toonen, S. 2021, *MNRAS*, 503, 4734
 Paxton, B., Bildsten, L., Dotter, A., et al. 2011, *ApJS*, 192, 3
 Pechetti, R., Seth, A., Kamann, S., et al. 2022, *ApJ*, 924, 48
 Perets, H. B., Badenes, C., Arcavi, I., Simon, J. D., & Gal-yam, A. 2011, *ApJ*, 730, 89
 Perets, H. B., Li, Z., Lombardi, James C., J., & Milcarek, Stephen R., J. 2016, *ApJ*, 823, 113
 Perley, D. A., Ho, A. Y. Q., Yao, Y., et al. 2021, *MNRAS*, 508, 5138
 Podsiadlowski, P., Rappaport, S., & Han, Z. 2003, *MNRAS*, 341, 385

- Portegies Zwart, S. F., Verbunt, F., & Ergma, E. 1997, *A&A*, 321, 207
- Prentice, S. J., Maguire, K., Smartt, S. J., et al. 2018, *ApJ*, 865, L3
- Press, W. H. & Teukolsky, S. A. 1977, *ApJ*, 213, 183
- Pursiainen, M., Childress, M., Smith, M., et al. 2018, *MNRAS*, 481, 894
- Reines, A. E. 2022, *Nature Astronomy*, 6, 26
- Rizzuto, F. P., Naab, T., Rantala, A., et al. 2023, *MNRAS*, 521, 2930
- Ryu, T., Amaro Seoane, P., Taylor, A. M., & Ohlmann, S. T. 2024a, *MNRAS*, 528, 6193
- Ryu, T., de Mink, S. E., Farmer, R., et al. 2024b, *MNRAS*, 527, 2734
- Ryu, T., Krolik, J., Piran, T., & Noble, S. C. 2020a, *ApJ*, 904, 98
- Ryu, T., Krolik, J., Piran, T., & Noble, S. C. 2020b, *ApJ*, 904, 99
- Ryu, T., Krolik, J., Piran, T., & Noble, S. C. 2020c, *ApJ*, 904, 100
- Ryu, T., Krolik, J., Piran, T., & Noble, S. C. 2020d, *ApJ*, 904, 101
- Ryu, T., McKernan, B., Ford, K. E. S., et al. 2024c, *MNRAS*, 527, 8103
- Ryu, T., Perna, R., Pakmor, R., et al. 2023a, *MNRAS*, 519, 5787
- Ryu, T., Perna, R., & Wang, Y.-H. 2022, *MNRAS*, 516, 2204
- Ryu, T., Valli, R., Pakmor, R., et al. 2023b, *MNRAS*, 525, 5752
- Salaris, M. & Weiss, A. 2002, *A&A*, 388, 492
- Sand, C., Ohlmann, S. T., Schneider, F. R. N., Pakmor, R., & Röpke, F. K. 2020, *A&A*, 644, A60
- Schneider, F. R. N., Ohlmann, S. T., Podsiadlowski, P., et al. 2019, *Nature*, 574, 211
- Schödel, R., Merritt, D., & Eckart, A. 2009, *A&A*, 502, 91
- Sądowski, A., Narayan, R., McKinney, J. C., & Tchekhovskoy, A. 2014, *MNRAS*, 439, 503
- Smartt, S. J., Clark, P., Smith, K. W., et al. 2018, *The Astronomer's Telegram*, 11727, 1
- Springel, V. 2010, *MNRAS*, 401, 791
- Stone, N. C., Kesden, M., Cheng, R. M., & van Velzen, S. 2019, *General Relativity and Gravitation*, 51, 30
- Stone, N. C., Küpper, A. H. W., & Ostriker, J. P. 2017, *MNRAS*, 467, 4180
- Timmes, F. X. & Swesty, F. D. 2000, *ApJS*, 126, 501
- Tonry, J. L., Denneau, L., Heinze, A. N., et al. 2018, *PASP*, 130, 064505
- Udalski, A., Szymański, M. K., & Szymański, G. 2015, *Acta Astron.*, 65, 1
- Voges, W., Aschenbach, B., Boller, T., et al. 1999, *A&A*, 349, 389
- Volonteri, M., Habouzit, M., & Colpi, M. 2021, *Nature Reviews Physics*, 3, 732
- Voss, R. & Gilfanov, M. 2007, *MNRAS*, 380, 1685
- Wang, Y.-H., Perna, R., & Armitage, P. J. 2021, *MNRAS*, 503, 6005
- Weinberger, R., Springel, V., & Pakmor, R. 2020, *ApJS*, 248, 32
- Weisskopf, M. C., Tananbaum, H. D., Van Speybroeck, L. P., & O'Dell, S. L. 2000, in *Society of Photo-Optical Instrumentation Engineers (SPIE) Conference Series*, Vol. 4012, *X-Ray Optics, Instruments, and Missions III*, ed. J. E. Truemper & B. Aschenbach, 2–16
- Xin, C., Haiman, Z., Perna, R., Wang, Y., & Ryu, T. 2024, *ApJ*, 961, 149
- Yao, Y., Ho, A. Y. Q., Medvedev, P., et al. 2022, *ApJ*, 934, 104
- Zauderer, B. A., Berger, E., Soderberg, A. M., et al. 2011, *Nature*, 476, 425

Appendix A: Summary of simulation results

Table A.1: Post-disruption parameter values for our 58 simulations.

	m_\star [M_\odot]	m_{BH} [M_\odot]	b	H_c	$L_\star / 10^{46}$ [$\text{g cm}^2 \text{s}^{-1}$]	m_\circ [M_\odot]	$m_{\star \rightarrow \text{BH}}$ [M_\odot]	m_{unbound} [M_\odot]	$L_\circ / 10^{48}$ [$\text{g cm}^2 \text{s}^{-1}$]	a [AU]	e
1	0.5	10.0	0.70	0.25	2	0.00	0.29	0.21	N/A	N/A	N/A
2	0.5	10.0	0.70	0.33	2	0.00	0.22	0.28	N/A	N/A	N/A
3	0.5	10.0	0.70	0.50	2	0.00	0.23	0.17	N/A	N/A	N/A
4	0.5	10.0	0.70	0.75	2	0.15	0.21	0.14	87	-0.07	1.06
5	0.5	10.0	0.70	1.00	2	0.25	0.14	0.11	97	-0.27	1.02
6	0.5	10.0	0.70	1.50	2	0.46	0.03	0.01	117	1.91	0.995
7	0.5	10.0	0.70	2.00	2	0.50	0.00	0.00	17	2.61	0.996
8	0.5	10.0	0.70	2.50	2	0.50	0.00	0.00	1	42.3	1.00
9	0.5	40.0	0.70	0.25	2	0.00	0.27	0.23	N/A	N/A	N/A
10	0.5	40.0	0.70	0.33	2	0.00	0.30	0.20	N/A	N/A	N/A
11	0.5	40.0	0.70	0.50	2	0.00	0.30	0.20	N/A	N/A	N/A
12	0.5	40.0	0.70	0.75	2	0.00	0.31	0.19	N/A	N/A	N/A
13	0.5	40.0	0.70	1.00	2	0.21	0.18	0.11	76	-0.35	1.03
14	0.5	40.0	0.70	1.50	2	0.46	0.03	0.01	110	-0.11	1.00
15	0.5	40.0	0.70	2.00	2	0.50	0.00	0.00	15	11.4	0.998
16	0.5	40.0	0.70	2.50	2	0.50	0.00	0.00	1	161	1.00
17	1.0	10.0	0.00	0.25	12	0.04	0.42	0.54	2	0.02	0.916
18	1.0	10.0	0.00	0.33	12	0.33	0.27	0.40	101	0.04	0.923
19	1.0	10.0	0.00	0.50	12	0.68	0.11	0.21	410	0.10	0.945
20	1.0	10.0	0.00	0.75	12	0.89	0.05	0.06	354	0.32	0.972
21	1.0	10.0	0.00	1.00	12	0.97	0.02	0.01	199	1.15	0.989
22	1.0	10.0	0.00	1.50	12	1.00	0.00	0.00	49	13.2	0.999
23	1.0	10.0	0.00	2.00	12	1.00	0.00	0.00	10	54.6	1.00
24	1.0	10.0	0.34	0.25	10	0.00	0.47	0.53	N/A	N/A	N/A
25	1.0	10.0	0.34	0.33	10	0.09	0.47	0.44	99	-0.06	1.12
26	1.0	10.0	0.34	0.50	10	0.49	0.20	0.31	245	0.08	0.950
27	1.0	10.0	0.34	0.75	10	0.83	0.09	0.08	440	0.21	0.965
28	1.0	10.0	0.34	1.00	10	0.95	0.03	0.02	250	0.64	0.984
29	1.0	10.0	0.34	1.50	10	1.00	0.00	0.00	49	7.77	0.998
30	1.0	10.0	0.34	2.00	10	1.00	0.00	0.00	10	87.3	1.00
31	1.0	10.0	0.70	0.25	16	0.00	0.37	0.63	N/A	N/A	N/A
32	1.0	10.0	0.70	0.33	16	0.00	0.49	0.51	N/A	N/A	N/A
33	1.0	10.0	0.70	0.50	16	0.34	0.29	0.37	163	0.28	0.986
34	1.0	10.0	0.70	0.75	16	0.68	0.16	0.16	440	0.2.2	0.968
35	1.0	10.0	0.70	1.00	16	0.90	0.06	0.04	387	0.35	0.974
36	1.0	10.0	0.70	1.50	16	1.00	0.00	0.00	67	3.43	0.996
37	1.0	10.0	0.70	2.00	16	1.00	0.00	0.00	8	25.5	0.999
38	1.0	40.0	0.00	0.25	12	0.07	0.45	0.48	56	-0.05	1.14
39	1.0	40.0	0.00	0.33	12	0.28	0.27	0.45	66	0.17	0.969
40	1.0	40.0	0.00	0.50	12	0.63	0.16	0.21	340	0.58	0.984
41	1.0	40.0	0.00	0.75	12	0.88	0.06	0.06	332	2.24	0.994
42	1.0	40.0	0.00	1.00	12	0.96	0.02	0.02	192	9.63	0.998
43	1.0	40.0	0.00	1.50	12	1.00	0.00	0.00	50	102	1.00
44	1.0	40.0	0.00	2.00	12	1.00	0.00	0.00	8	153	1.00
45	1.0	40.0	0.34	0.25	10	0.00	0.42	0.58	N/A	N/A	N/A
46	1.0	40.0	0.34	0.33	10	0.00	0.39	0.61	N/A	N/A	N/A
47	1.0	40.0	0.34	0.50	10	0.42	0.22	0.36	169	0.95	0.992
48	1.0	40.0	0.34	0.75	10	0.81	0.09	0.10	413	1.84	0.993
49	1.0	40.0	0.34	1.00	10	0.95	0.03	0.02	245	5.09	0.997
50	1.0	40.0	0.34	1.50	10	1.00	0.00	0.00	50	62.6	1.00

51	1.0	40.0	0.34	2.00	10	1.00	0.00	0.00	10	180	1.00
52	1.0	40.0	0.70	0.25	16	0.00	0.55	0.45	N/A	N/A	N/A
53	1.0	40.0	0.70	0.33	16	0.00	0.50	0.50	N/A	N/A	N/A
54	1.0	40.0	0.70	0.50	16	0.21	0.39	0.40	156	-0.12	1.06
55	1.0	40.0	0.70	0.75	16	0.63	0.18	0.19	365	-4.17	1.00
56	1.0	40.0	0.70	1.00	16	0.89	0.06	0.05	368	2.91	0.995
57	1.0	40.0	0.70	1.50	16	1.00	0.00	0.00	66	29.4	0.999
58	1.0	40.0	0.70	2.00	16	1.00	0.00	0.00	8	119	1.00

Notes. The columns, respectively, denote star mass m_* , BH mass m_{BH} , impact parameter b , central hydrogen abundance H_c , initial (almost non-rotating) star spin angular momentum L_* , remnant mass m_\circ , gas mass bound to BH $m_{*\rightarrow\text{BH}}$, gas mass unbound from the BH-star system m_{unbound} , remnant spin angular momentum L_\circ , orbital semimajor axis a and orbital eccentricity e .